

Article

A Novel Bidirectional DC–DC Converter with Low Stress and Low Magnitude Ripples for Stand-Alone Photovoltaic Power Systems

Alamdar Hussain ^{1,2}, Rizwan Akhtar ^{1,*} , Babar Ali ², Saeed Ehsan Awan ² and Shahid Iqbal ³

¹ School of Electronics and information, Jiangsu University of Science and technology, Zhenjiang 212003, China

² Department of Electrical Engineering, COMSATS University Islamabad, Attock Campus, Attock 43600, Pakistan

³ Department of Electrical Engineering, University of Gujrat, Gujrat 50700, Pakistan

* Correspondence: rizwan@just.edu.cn

Received: 19 June 2019; Accepted: 15 July 2019; Published: 26 July 2019



Abstract: Photovoltaic (PV) power is one of the promising solutions to address the fast-growing electricity demand. Electricity generated from the array of solar panels is not fixed due to the continuous change in environmental conditions. Therefore, an efficient power management system is required to facilitate the consumer with an uninterruptable power supply (UPS). When the energy demand is lower than the energy generated by the PV power system, the excessive energy must be stored in batteries and, when the energy demand is higher than the energy generated by the PV system, then the stored energy in the battery must be released in order to fulfil the load demand. Therefore, a bidirectional DC–DC converter is required to store and release energy. Conventional bidirectional converters offer low gain, low power density, low efficiency, high switching stress, and high magnitude of current and voltage ripples. In this paper, a bi-directional DC–DC converter that has low stress and low ripples is proposed for the operation of Stand-alone PV power systems. The proposed converter is implemented in ORCAD/PSPICE (Oregon Computer Aided Design/Personal Computer Simulation Program with Integrated Circuit) and both the charging and discharging modes have been analyzed explicitly. The results were compared with conventional converters and were found to be satisfactory. A significant improvement in the magnitude of output voltage and current ripples has been noticed. Besides, considerable improvement in switching stress (45% reduction as compared with conventional converters) and a 16.6% reduction in the magnitude of ripples was realized.

Keywords: bidirectional DC–DC converter; PV power system; UPS; switching stress; voltage and current ripples

1. Introduction

Energy from renewable sources has become the best solution to address ecological pollution as well as the increase in power demand all over the world. To date, most of the energy that we use is directly or indirectly from the burning of fossil fuels, which greatly affects the global environment [1]. Solar photovoltaic (PV) power shows great potential among the other renewable energy sources, by providing clean, noise-free and contamination-free energy conversion [2]. However, in order to utilize solar energy, power electronic converters are essential. This is because the output voltage of a single solar panel is usually in the range of 18–22 V. The low output voltage of a solar panel needs to be raised to 350–400 V before supplying to DC–AC inverters, which produce AC output power. There are two types of power conversion circuits: single-stage conversion circuits and double-stage conversion circuits [3]. Our focus is on the latter, which use a DC–DC converter to feed into the inverter. There are

many types of DC–DC converters such as PWM (Pulse Width Modulation) switch-mode DC–DC converters, zero-voltage zero-current switching DC–DC converters, boost converters, buck converters and resonant converters [4]. The focus of this research work is on the development of PWM switch-mode high-gain DC–DC converters as the first stage of PV power systems. Stand-alone PV power systems are useful in remote and isolated areas to where the power grid cannot be extended. Stand-alone PV power systems are of much importance for rural areas where it is not Possible or uneconomical to get connect with the Grid Figure 1 shows the block diagram of stand-alone PV power systems, which consists of an array of solar cells, a unidirectional boost converter, a single-phase DC–AC inverter, a storage battery and, most importantly, a bi-directional DC–DC converter. The solar array is connected with the DC bus through the unidirectional DC–DC converter and the battery is also connected with the DC bus through the bidirectional DC–DC converter. Most home appliances operate on AC. Therefore, the DC voltages at the DC bus are converted in AC through the PWM inverter. Stand-alone PV power systems are an important source of electricity for domestic applications—especially in Pakistan, where energy crises are being faced. By developing stand-alone power systems that are independent of utility, electricity consumers can generate electricity themselves. Bidirectional DC–DC converters used in stand-alone PV power systems must have the following properties: high DC gain, low stress on power switches, low electromagnetic interference (EMI), high power density, and a low magnitude of output voltage and current ripples. When power is being transferred from the battery to the load, it requires a high voltage gain ratio where conventional bidirectional converters provide high voltage gain at the cost of low circuit efficiency. This low efficiency is caused due to the high switching stress of the semiconductor switch operated in heavy duty cycles. Besides low efficiency and high switching stress, conventional bidirectional converters also produce electromagnetic interference (EMI) to nearby communication systems. The output voltage and current of conventional converters contain a high magnitude of ripples, which is also undesirable for a DC–DC converter [5,6]. There is a trade off in PWM converters between gain and efficiency. The aim of this research is to explore and design a novel bidirectional converter that can perform well in terms of efficiency, cost, gain, size, and maximizing the lifetime of storage batteries.

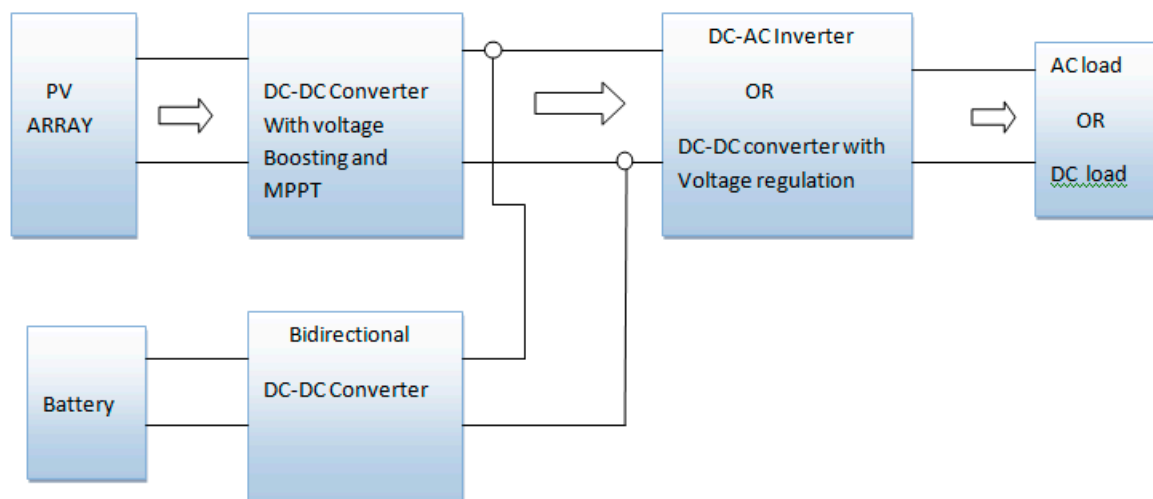


Figure 1. Block diagram of stand-alone PV power systems [7].

2. Related Work

There has been much research on renewable energy source yield and stand-alone PV power systems as well as grid-connected PV power systems. Power conditioning is an important process to match the electric load demand with the power generated from PV panels. Bidirectional DC–DC converters play an important role in both the stand-alone mode and grid-connected mode. To increase the efficiency of stand-alone PV power systems, different techniques are used—one of which is

to make the bidirectional converter as efficient as possible in terms of cost, maximum power point tracking (MPPT), reduction in the size of the transformer, and reduction in the magnitude of ripples, as well as placing low stress on the power switches, and high voltage gain with high efficiency. Conversion systems without an isolation transformer are referred to as non-isolated DC–DC converters—usually, these conversion systems are either of the boost type or buck type. Conversion systems based on a high-frequency transformer are an attractive approach to attain isolation among the load and source sides. However, if renewable energy sources are considered like photovoltaic (PV) power systems and wind energy power systems, their energy production is very low. Therefore, non-isolated conversion systems are considered to be much more attractive [8]. Low weight, low cost, and high efficiency are the other advantages of non-isolated DC–DC converters over isolated DC–DC conversion systems [9–11]. In order to increase power density for bidirectional converters, multiphase current interleaving technology with minimized inductance has been found in the literature [12,13]. Better efficiency as well as low current stress on devices are the two main features in bidirectional DC–DC converters, which is reported to be found in multiphase converter circuits [14]. Coupled inductor-based non-isolated converters with a high gain ratio have been presented in [15–17]. Interleaved high step-up converters which are composed of a general boost converter with a switched capacitor have been proposed in [18,19]. A new family of DC–DC converters based on winding-cross-coupled inductors (WCCIs) have been introduced in [20,21], modifying the existing coupled inductor structure by a third winding of the coupled inductor that is inserted into the next phase also called WCCI [22]. Inclusion of tertiary winding causes the size of Coupled Inductor hulk as well as it boosts the complexity of the circuit. Extra winding results increase in winding losses, core losses and the cost. Furthermore, the switches are exposed to high voltages, which results in high conduction losses. One of the important parts of stand-alone PV power systems are the storage batteries used [23]. A topology of bidirectional converters based on zero-current switching (ZCS), quasi-resonant (QR) and switched-capacitor (SC) technology is presented in [24]. This converter consists of four main switches that are antiparallel with high-frequency diodes. To construct a resonant tank, a set of MOSFET (Metal-oxide-semiconductor field effect transistors and a capacitor are connected in series with the small inductor). This topology is suitable for low-gain applications. However, it consists of a total number of nine switches, which creates the complexity of the circuit as well as the conduction losses that occur in MOSFETs. One of the prominent methods to reduce the conduction losses of semiconductor switches and increase their circuit efficiency is distributing the power in multiple phases as a dual-phase split-buck boost. This topology provides a very low magnitude of ripples at the output and also provides a reduction in the stress on the battery and the output capacitor respectively [25]. However, this schematic consists of eight numbers of switches, which increases the complexity of the circuit as well as the losses. Leakage energy of the inductor is also not recycled. Therefore, its efficiency decreases. DC–DC converters for micro grids [26–31] have limitations in high power applications as well as in the transfer of power—unidirectional only. The above analysis requires the design of a novel high-gain, high-efficiency bidirectional DC–DC converter, with a low magnitude of current and voltage ripples and low current stress on the power switches for stand-alone PV power systems application.

3. Proposed Bidirectional DC–DC Converter

Figure 2 shows the circuit diagram of a proposed two-phase bidirectional DC–DC converter. It is formed by the incorporation of an additional phase from the high efficiency, high-gain converter in [7]. The proposed converter topology is based on the concept of the intermediate storage capacitor and coupled inductor in order to increase its efficiency and output voltage simultaneously. The proposed converter is a two-phase converter, based on a coupled inductor, clamped circuit, output capacitor and an intermediate capacitor for each phase, and it has the additional features of a low magnitude of ripples, with high voltage gain and high efficiency. This bidirectional converter is seen to have a two-phase circuit for the boost mode of operation, while a simple DC–DC converter is used to operate

in the buck mode. The battery voltages are stepped up to transfer the power from battery to high voltage DC link (V_{bus}), whereas the voltages of V_{bus} are stepped down to store the power in the battery. Power switches (s_1, s_2) will operate the stepped up voltages, while power switch (s_3) will operate the stepped down DC-link voltages.

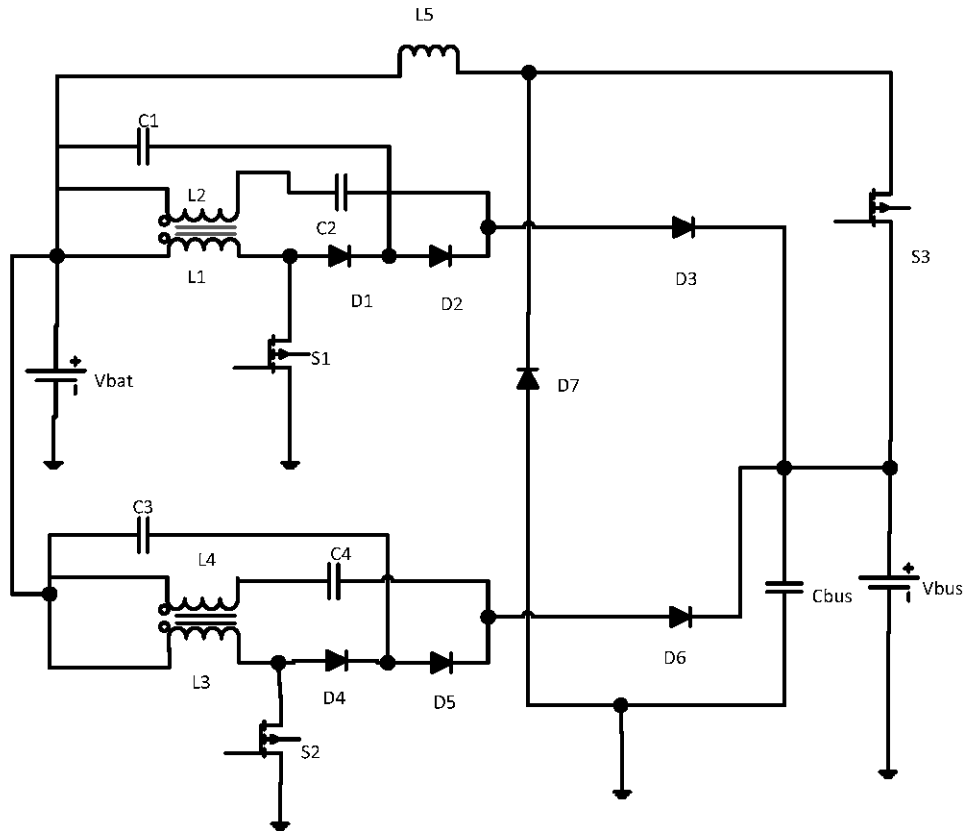


Figure 2. Proposed bidirectional DC–DC converter.

3.1. Analysis of the Steady-State Operation

3.1.1. Step-Down Mode

To step down the voltages from the high voltage DC-link, the power switch (s_3), diode D_7 and inductor will operate. The circuit diagram for the buck mode of operation is highlighted in Figure 3.

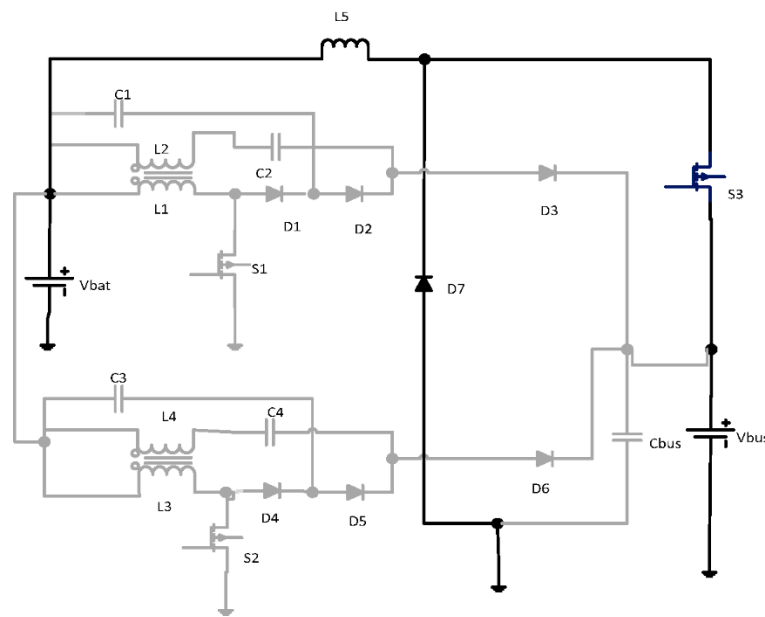


Figure 3. Step-down converter.

Mode 1 (Switch closed)

When Switch (s_3) is closed, the current I will flow through the inductor L_5 , while diode D_7 will act as an open switch as shown in Figure 4. By applying KVL(Kirchoff's Voltage Law) to the circuit in Figure 3, Equation (1) is found.

$$v_l = v_{bus} - v_{bat} \tag{1}$$

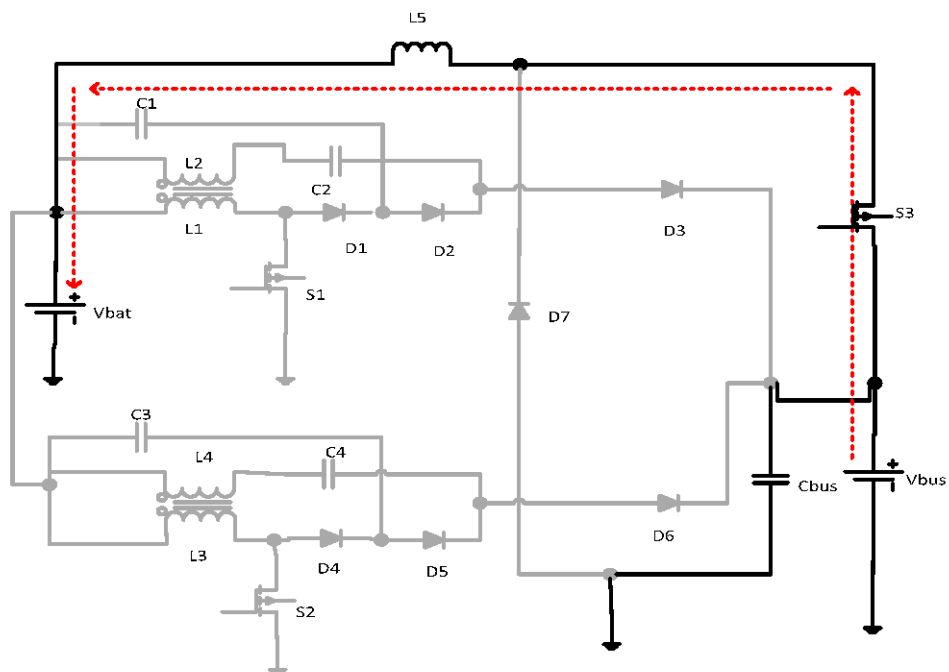


Figure 4. Mode 1 (switch closed).

Mode 2 (Switch open)

When switch S_3 is opened, the inductor will reverse its polarities and release the stored energy through diode D_7 , as shown in Figure 5.

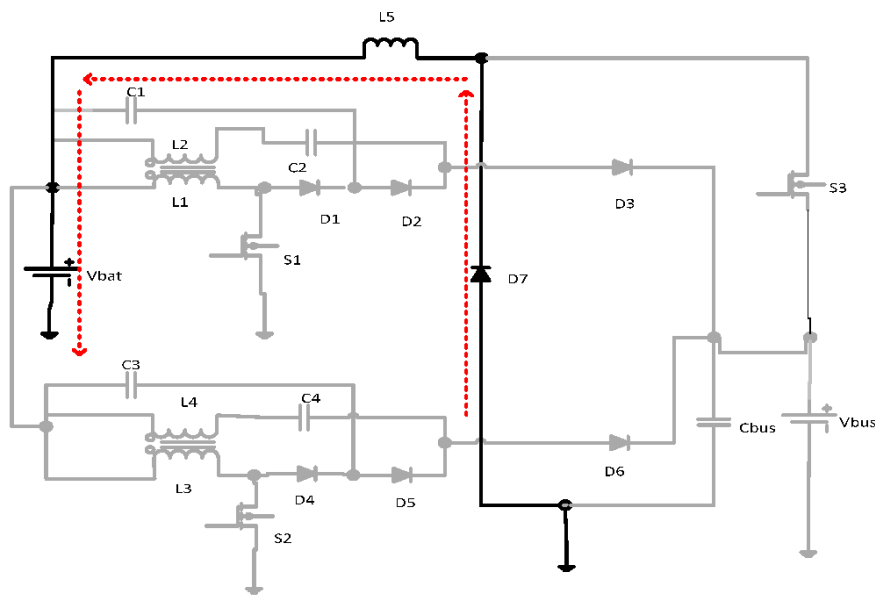


Figure 5. Mode 2 (switch opened).

When the switch is open,

$$v_l = v_{bat} \quad (2)$$

Applying Volts seconds balance to the inductor L_5 ,

$$v_l \times t_{on} = v_l \times t_{off} \quad (3)$$

$$(v_{bus} - v_{bat}) \times t_{on} = (v_{bat} \times t_{off}) \quad (4)$$

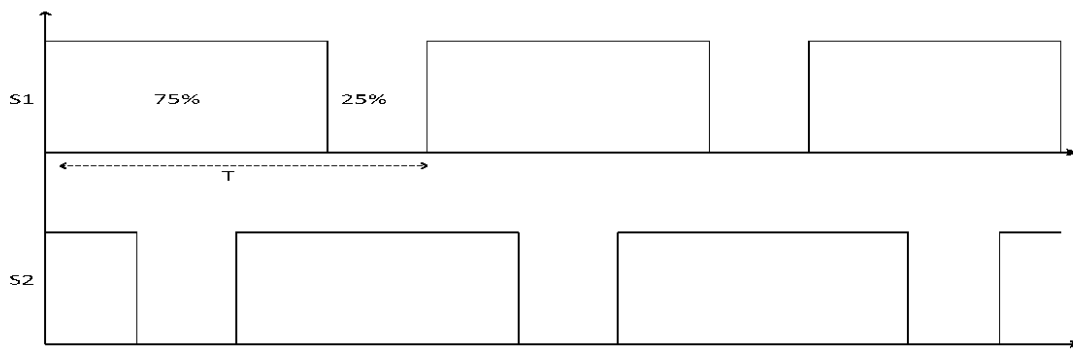
Dividing both sides by T_S , we obtain the final equation given by (5),

$$v_{bat} = D \times v_{bus} \quad (5)$$

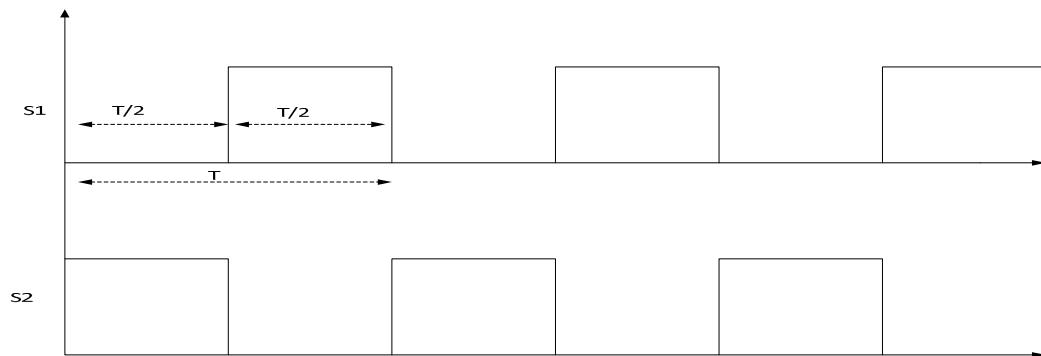
where D is the duty cycle, which can be varied theoretically from 0 to 100%.

3.1.2. Step-Up Mode

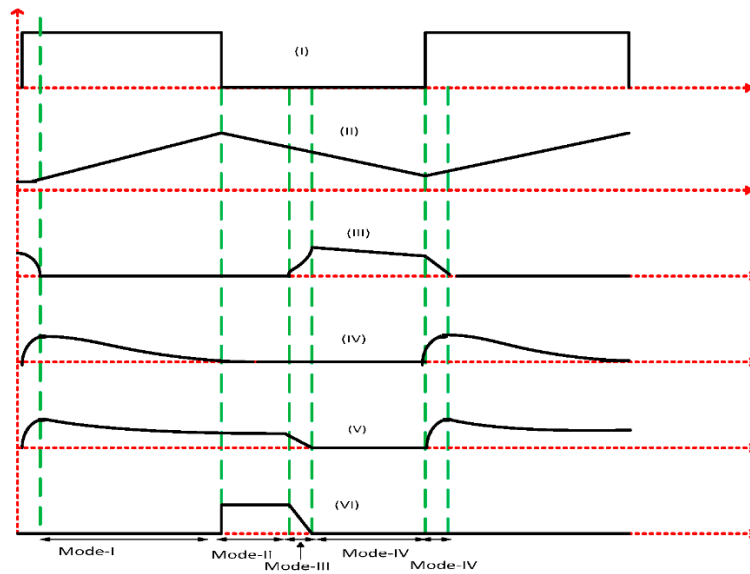
We considered the power switches as ideal switches in this analysis. In addition, we considered the capacitors and inductors as ideal by neglecting the parasitic resistances. Equations of the boost mode of operation at different switching states are presented with the help of circuit diagrams. In this topology, two phases with similar components have been interleaved. Considering the continuous conduction operation of each of the two phases gives five different modes. Each mode has been shown using circuit diagrams. Switching signals for both the switches for the boost mode of operation are shown in Figure 6a,b for a 75 and 50% duty cycle. However, it can be varied. In this analysis, s_2 is initially off while s_1 is open, then s_2 is closed while s_1 is open.



(a)



(b)



(c)

Figure 6. Cont.

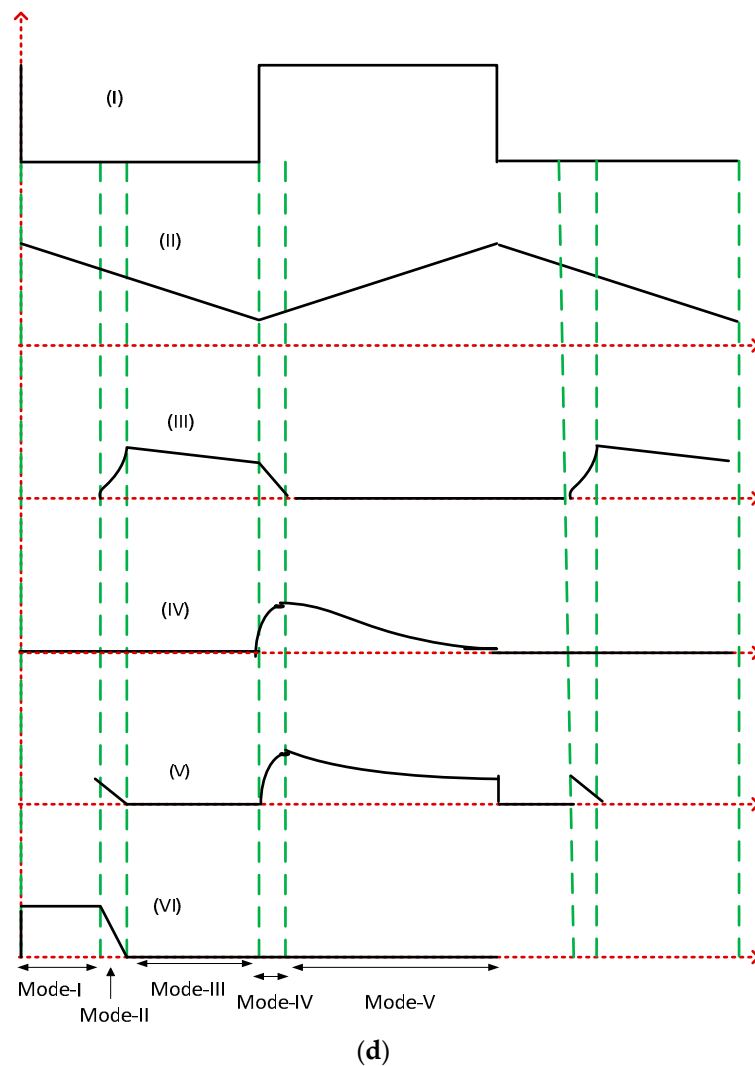


Figure 6. (a) Switching signal for a 75% duty cycle. (b) Switching signal for a 50% duty cycle. (c) Waveforms for the continuous conduction mode (Phase I): (i) Switching signal; (ii) Magnetizing inductance current; (iii) Current through D_3 ; (iv) Current through diode D_2 ; (v) Primary inductor L_1 current; (vi) Current through diode D_1 . (d) Waveforms for the continuous conduction mode (Phase II): (i) Switching signal; (ii) Magnetizing inductance current; (iii) Current through D_6 ; (iv) Current through diode D_5 ; (v) Primary inductor L_3 current; (vi) Current through diode D_4 .

Mode I

In this mode of operation, a gate signal is applied to switch S_1 , which is turned on completely from the off mode. By turning on the switch as shown in Figure 7, the magnetizing current starts to flow through the primary side of the coupled inductor in a linearly incremental way. Capacitor C_2 is charged by the magnetizing current flowing through the secondary side of the coupled inductor. Diode D_2 and capacitor C_1 which forms a clamped circuit is also in series connection with capacitor C_2 . When the current of the leakage inductor decreases to zero, diode D_2 goes into the off state. The voltage across the primary inductor at the end of this mode will become equal to the applied battery voltages. In this mode, s_1 is closed and s_2 is open as shown in Figure 6.

$$v_{l1} = v_{bat} \quad (6)$$

$$v_{c2} = v_{c1} + v_{l2} \quad (7)$$

$$v_{l3} = -v_{C3} \quad (8)$$

Mode II

Switch S_1 is changed from the conduction state to the off state in this mode of operation. Figure 8 shows that diode D_3 is in the reverse bias mode and diode D_1 is in the forward bias mode. The energy that is stored in the primary side of the coupled inductor is transferred to the capacitor via diode D_1 . Inductor has the property to oppose the change in current therefore the current will continuously flow in the same direction until the secondary side of coupled inductor is fully discharged. This mode of conduction will change when Diode D_2 goes into non conduction state.

Mode III

In this mode of operation, diode D_2 is in the off state with switch S_1 . Diodes D_1 and D_3 are in the conducting state. Figure 9 shows the path of the current in dotted lines. The stored energy on the primary side of the coupled inductor is released to capacitor C_1 , operating as a clamped capacitor. Energy from battery source is stored in capacitor C_2 and the stored energy in the secondary winding of coupled inductor is then transferred to the DC bus through diode D_3 in this mode. As shown in Figure 9, all three energy sources in this case are connected together in series. Therefore, we get:

$$v_{l1} = -v_{C1} \quad (9)$$

Applying KVL(Kirchhoff's Voltage Law) on the outer loop of Phase I

$$v_{l2} = v_{bat} + v_{C2} - v_o \quad (10)$$

Similarly, in this mode, the current is also being fed through Phase II. Therefore,

$$v_{l4} = v_{bat} + v_{C4} - v_o \quad (11)$$

Mode IV

In this mode of operation, diodes D_1 and D_2 are in the off state. Switch S_1 is also in the off state. Figure 10 shows how the current is flows through the secondary side of the coupled inductor, capacitor C_2 and diode D_3 towards the load. The current flow through Phase II has also been highlighted with dotted lines.

$$v_{l3} = v_{bat} \quad (12)$$

Mode V

Figure 11 shows the direction of the current in this mode of operation. Switch S_1 is now turned on from the off state to the on state. Here, it seems that diode D_3 is conducting, while diodes D_1 and D_2 are not conducting. The current from the battery source will complete its path through the primary side of the coupled inductor and switch. When the current through the secondary side of the inductor becomes zero, this mode will change and the cycle will repeat by starting from Mode I. Here, applying KVL on the inner loop of Phase II

$$v_{c4} = v_{c3} + v_{l4} \quad (13)$$

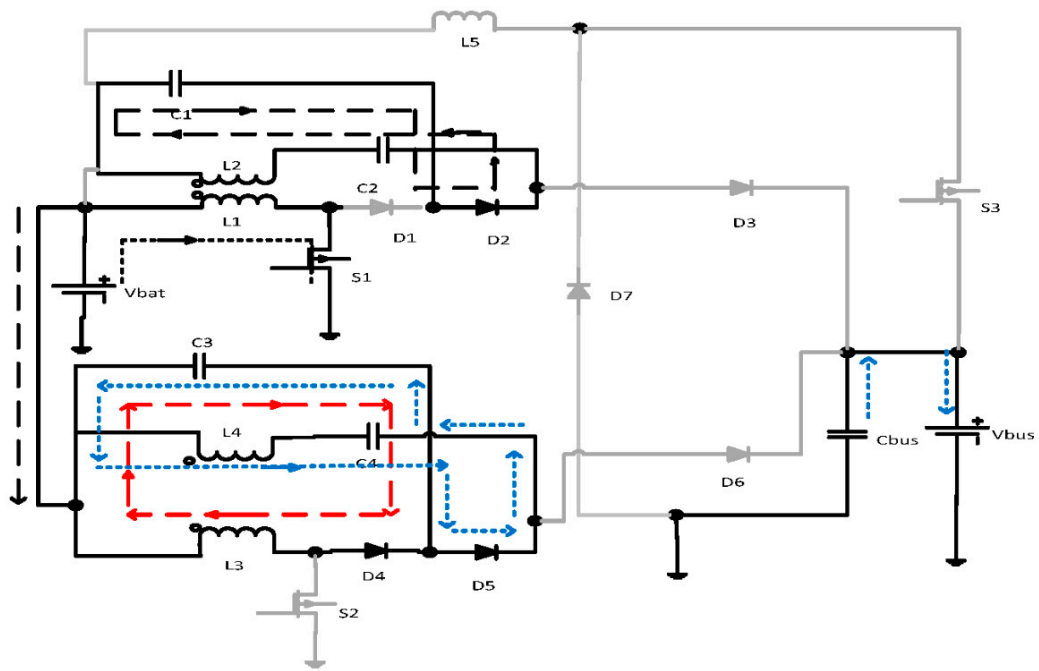


Figure 7. Mode I of operation.

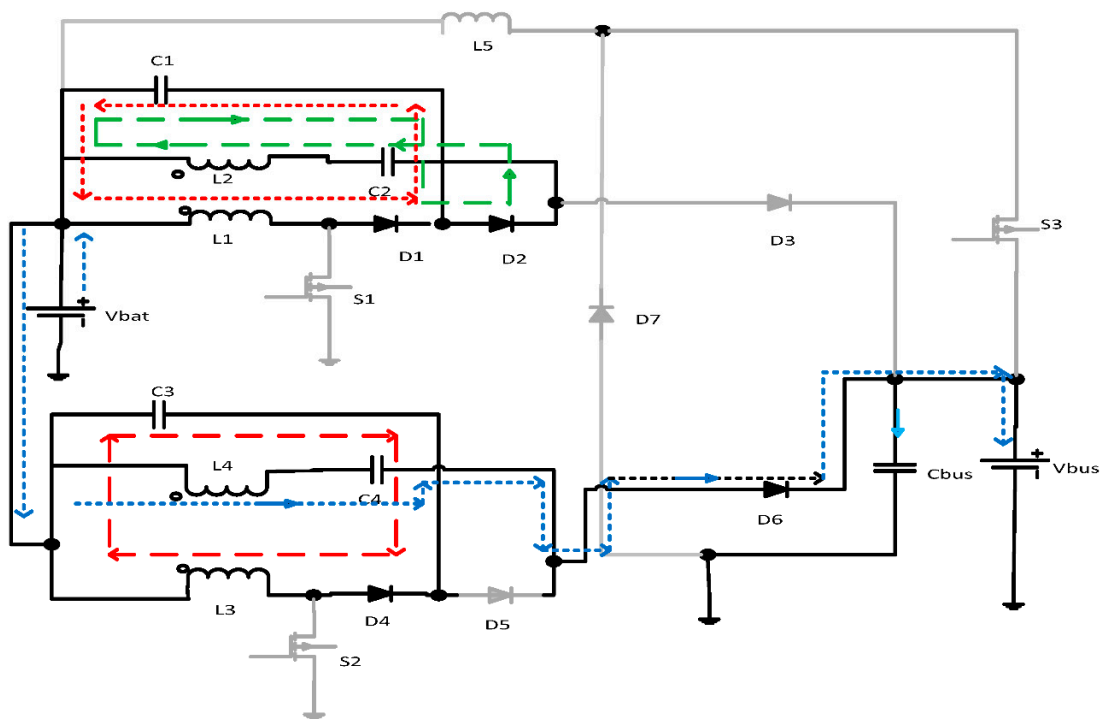


Figure 8. Mode II of operation.

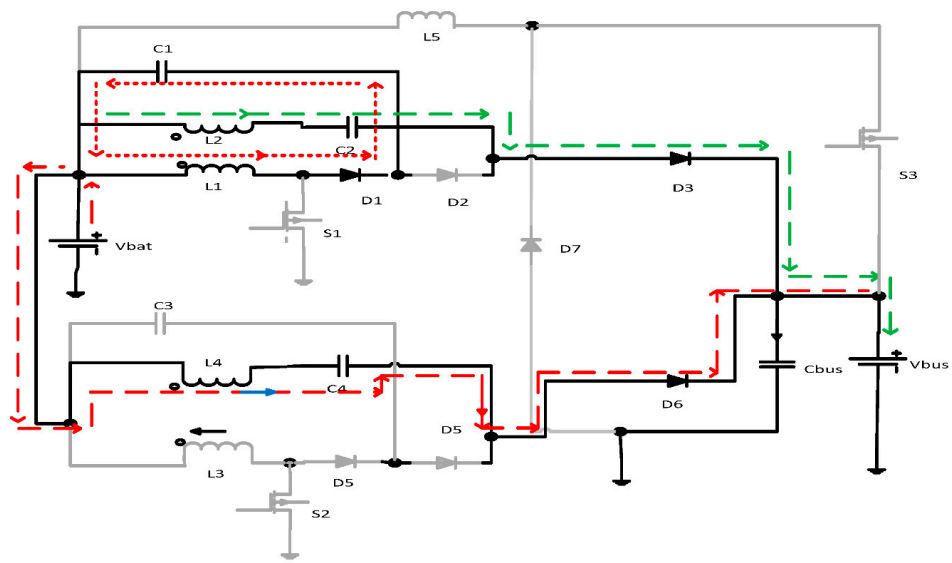


Figure 9. Mode III of operation.

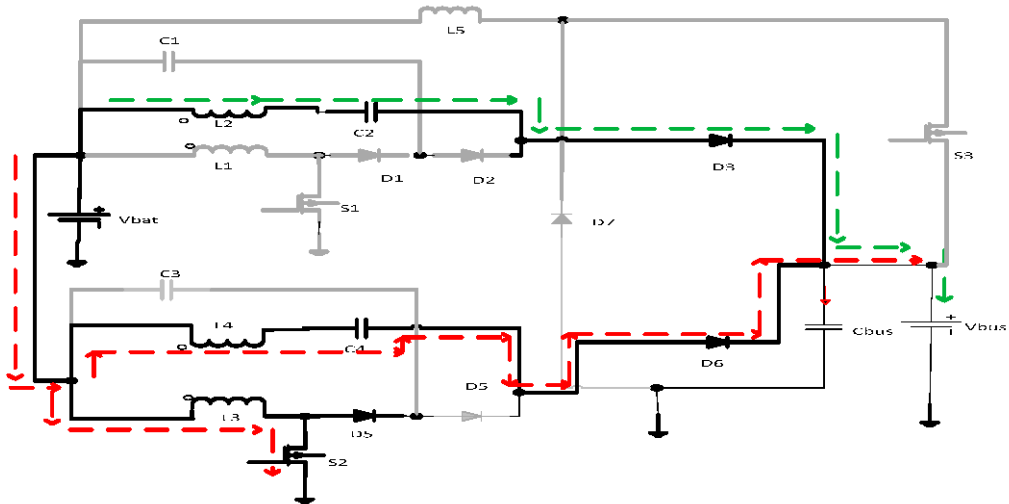


Figure 10. Mode IV of operation.

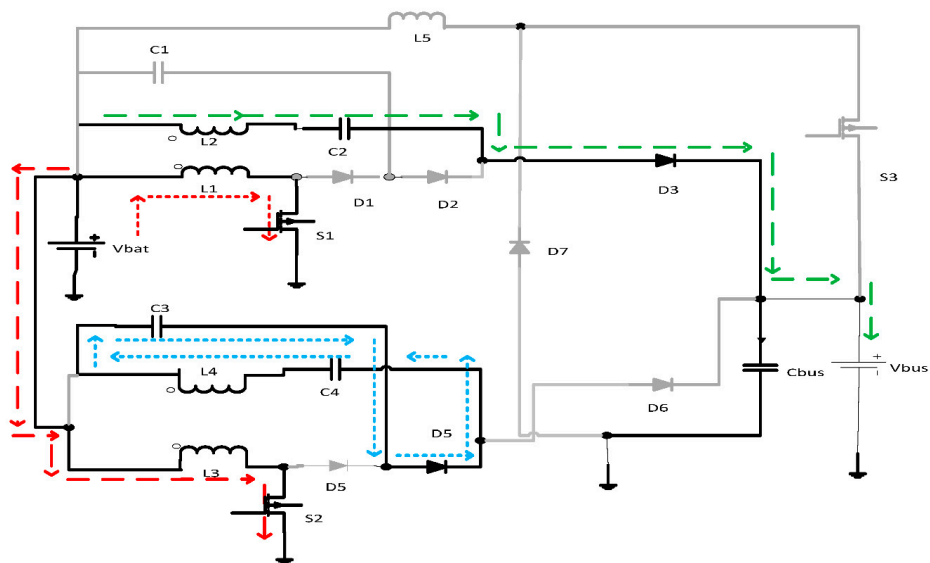


Figure 11. Mode V of operation.

3.2. Gain Analysis

Since the proposed topology is a two-phase converter topology, both the phases consist of components of the same specifications and are identical. In addition, both the switches s_2 and s_1 operate at the same duty cycle. So, the gain analysis for any one phase will be identical for the same other phase. Both the phases are operating parallel; so, the overall voltage gain at the output of one phase will not be affected by the voltage gain of the other phase.

The turn ratio of the coupled inductor can be determined as

$$n = \frac{v_{l2}}{v_{l1}} = \frac{v_{l4}}{v_{l3}} \quad (14)$$

Deriving an expression for phase 1,

Applying Volts-seconds balance on the primary windings of inductor L_1

$$v_{l1} \times D + v_{l1} \times (1 - D) = 0 \quad (15)$$

$$v_{c1} = (D) / (1 - D) \times v_{bat} \quad (16)$$

$$v_{c2} = \left(\frac{D}{1 - D} \times v_{bat} + n \times v_{l1} \right) \quad (17)$$

$$v_{l2} = + \left(\frac{D}{1 - D} \times v_{bat} + n \times v_{bat} \right) - v_o \quad (18)$$

$$v_{bat} \times D + \frac{\left(v_{bat} + \left(\frac{D}{1 - D} \times v_{bat} + n \times v_{bat} \right) - v_o \right)}{n} \times (1 - D) = 0 \quad (19)$$

Similarly, Phase I and Phase II are identical to each other. Therefore, the final equation for voltage gain is achieved as:

$$\frac{v_o}{v_{bat}} = \frac{n + 1}{1 - D} \quad (20)$$

However, the stress on the power switches is given by

$$s = t_{on} v_{max} I_{max} \quad (21)$$

where:

' n ' is the turn ratio of the coupled inductor L_3 and L_4 .

' D ' is the duty cycle of the gate signal applied to switch S_2 .

' s ' denotes the stress on switches.

' V_{max} ' is the voltage across the switch when the switch is in the off mode.

' I_{max} ' is the current flowing through the switch when it is in the conduction mode.

' t_{on} ' is the duration for which the switch is closed.

4. Design Considerations

The proposed converter topology is designed for a load of 300 W keeping in mind the DC bus link is operated in the range of 380–400 V. When the bidirectional converter is operated in the buck mode, it will store the energy in a battery bank. Initial parameters for the proposed DC–DC converter are based on the operation of stand-alone PV power systems—in which, the storage battery bank is operated at different voltages. Commercially available batteries have a rated voltage of 12 V. However, these batteries are connected in series and parallel combinations to operate at different voltage levels. The battery bank operating voltage of nearly every stand-alone PV power systems is around 40 Volts. The coupled inductor design is of the utmost importance. Hence, it can be designed by a flow chart. The proposed converter is implemented and simulated in ORCAD/PSPICE. Figure 12

shows the boost mode implementation and Figure 13 shows the implementation of the buck mode in ORCAD.

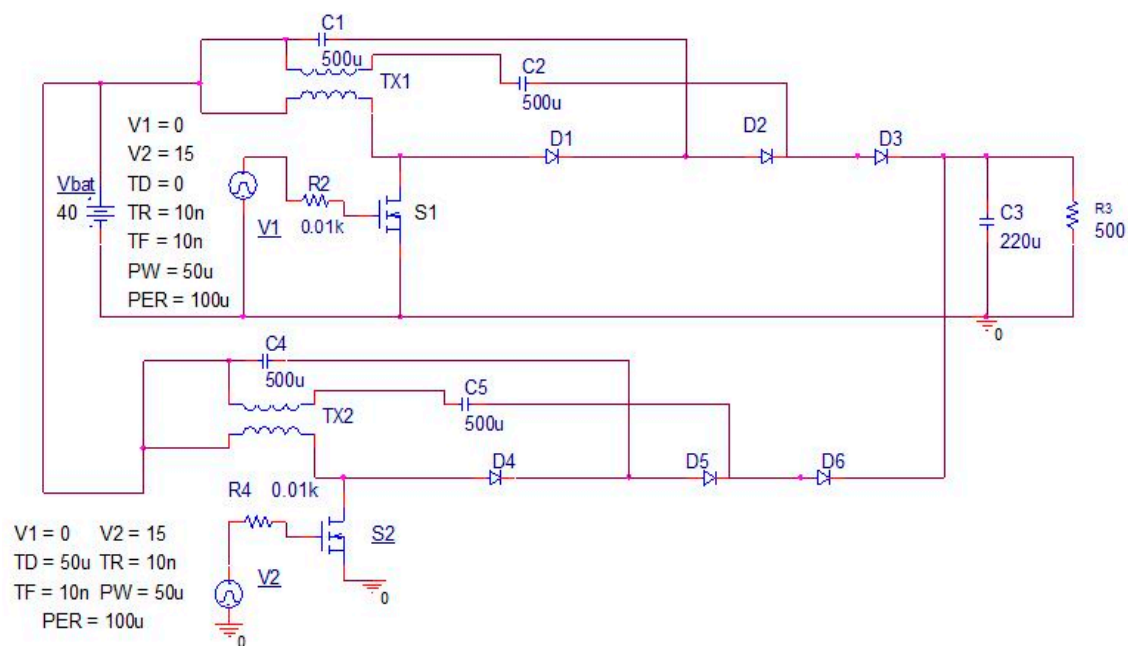


Figure 12. Boost mode.

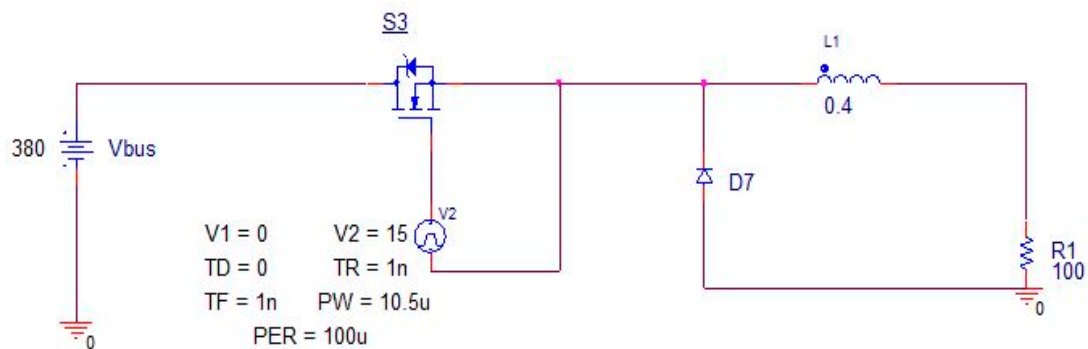


Figure 13. Buck mode.

The proposed converter topology has been designed for the initial design parameters of Table 1.

Table 1. Design Parameters.

Parameters	Values
Input Voltage	40 V–50 V
Output Voltage	380 V–400 V
Rated Power	285 W
Switching Frequency	10 KHz
Number of Primary Turns of coupled Inductor	48 turns
Number of Secondary Turns of coupled Inductor	225 turns

5. Losses in Converter

For the design parameters in Table 1, we have chosen NTB35N15 N-Channel MOSFET (Metal-oxide Semiconductor field effect transistor) as switching device which is rated as

$$V_{DSS} = 150 \text{ V}, I_{Dmax} = 37 \text{ AMPERES}, R_{DS} = 50 \text{ m}\Omega$$

5.1. Conduction Losses

$$P_{(on)} = I_{D(on)}^2 \times R_{DS(on)} \times \frac{t_{on}}{T} \quad (22)$$

$$P_{(on)} = 22.5 \text{ W}$$

5.2. Dynamic or Inductive Losses

$$P_{dynamic,inductive} = \frac{V_{DD} \times I_{D(on)}}{2T} (T_{on} + T_{off}) \quad (23)$$

$$P_{dynamic,inductive} = 23.25 \text{ W}$$

5.3. Magnetic Losses

The magnetic losses in DC–DC converters occur due to inductive elements. When the voltage across the inductor is in the form of a square wave, the magnetic loss can be determined using Equation (24) [32].

$$P_{magnetic\ loss} = C_1 \times B^{C_2} \times f^{C_3} \times D^{C_4} \times (1 - D)^{C_5} \quad (24)$$

where C_1, C_2, C_3, C_4, C_5 are constants.

In order to select an optimum size of coupled inductor core for the load requirements of Table 1 EFD20 is suitable having constants in Equation (25)

$$P_{magnetic\ loss} = 8.89 \times 10^{-7} \times B^{1.923} \times f^{1.503} \times D^{-0.512} \times (1 - D)^{-0.585} \quad (25)$$

From Equation (25), it is clear that magnetic losses are at a minimum for a 50% duty cycle, which was the operating duty cycle for the proposed converter.

6. Results and Discussion

In the previous sections, we analyzed the proposed topology mathematically in terms of voltage gain, magnitude of output voltage ripples, magnitude of output current ripples and component stress. This section describes the verification of the mathematical analysis with its simulated results in ORCAD/PSPICE. Finally, the results will be compared with the results of conventional converters. The results of the proposed bidirectional converter will be presented in two stages. In the first stage, the results for the boost mode operation of the converter will be discussed and then the results of the buck mode of operation will be presented and discussed.

6.1. Boost Mode

For stand-alone PV power systems, the voltages at the DC bus must be in the range of 380 to 400 V while the input voltage should be in the range of 40 to 50 V. The storage batteries that are commercially available have the voltage ratings of 12 V. However, these voltages are connected in series to provide an input voltage of 40 to 50 V. One of our desired outcomes is that, when the converter with bidirectional power flow is operated in the boost mode, then its voltage gain must be high enough to meet the voltage level of the DC link without exposing the power switches for extreme duty cycles. Figure 14 shows the output voltage of the boost mode of operation by setting the turn ratio of the coupled inductor to four and operating it for a 50% duty cycle. Theoretically, the voltage at the output terminal should be 400 V. Figure 14 is the proof of the mathematical design in which each of the switches are operated for a 50% duty cycle. The output current of the boost mode is shown in Figure 15, in which the voltage across the load is 400 V for a resistive load of 560 Ω selected by keeping in mind a load of 285 W.

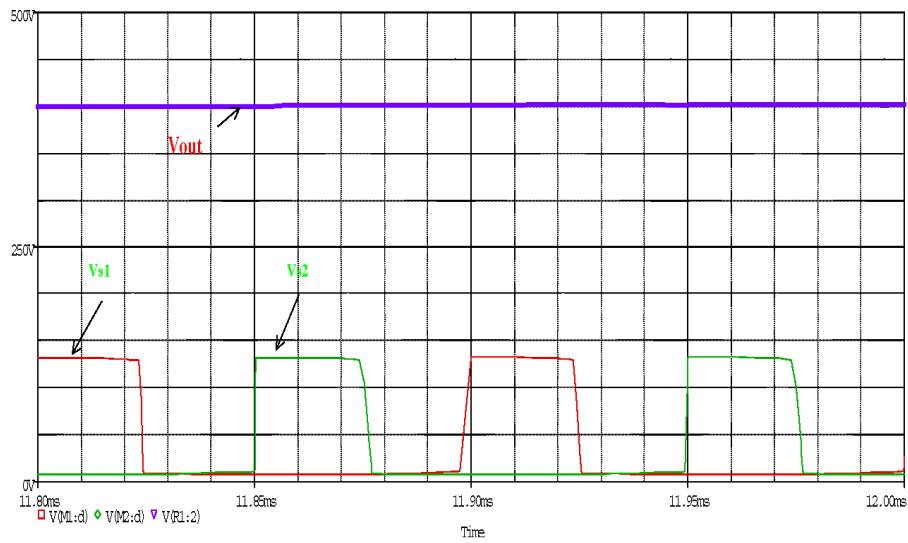
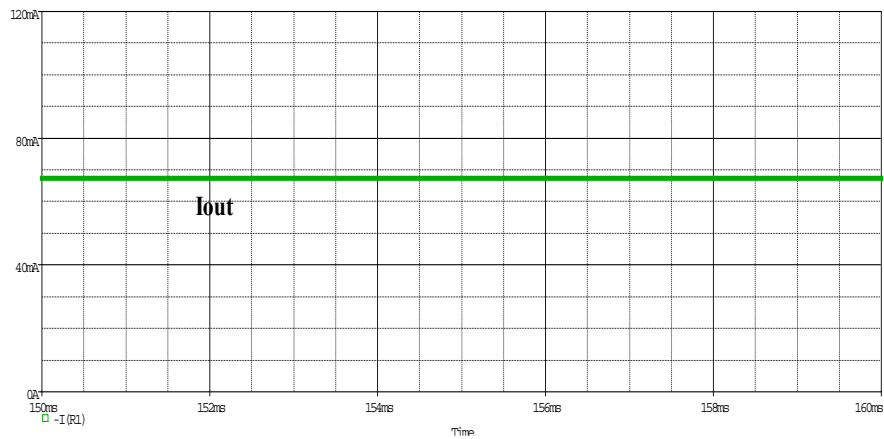
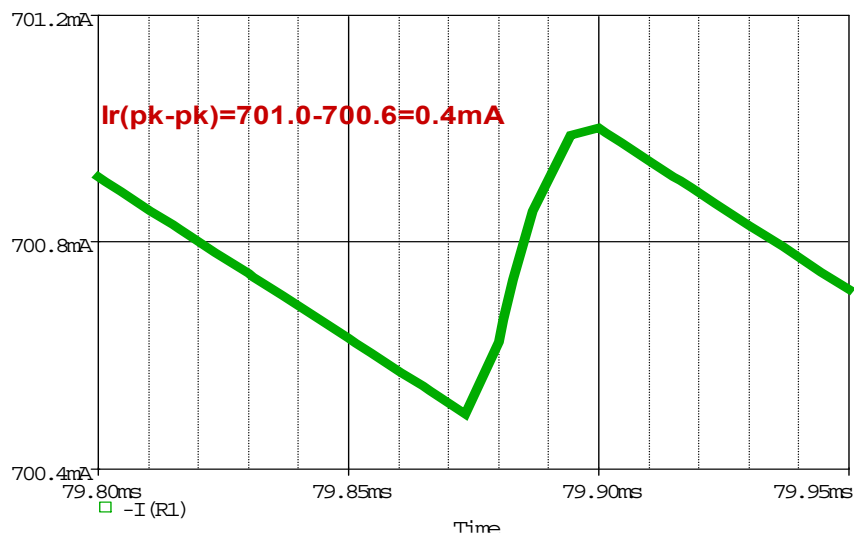


Figure 14. Output voltage waveform across load and voltages across switches.



(a)



(b)

Figure 15. (a) Output current waveform. (b) Magnitude of output ripples for proposed converter.

L_1 is the primary winding of the coupled inductor of Phase I, while L_3 corresponds to the primary winding of the coupled inductor of Phase II. We have selected similar coupled inductors with the same

turn ratio for both phases and also operated both the phases at the same frequency and same duty cycle. Figures 16 and 17 show that both L_1 and L_3 have the same behavior in terms of voltage and current.

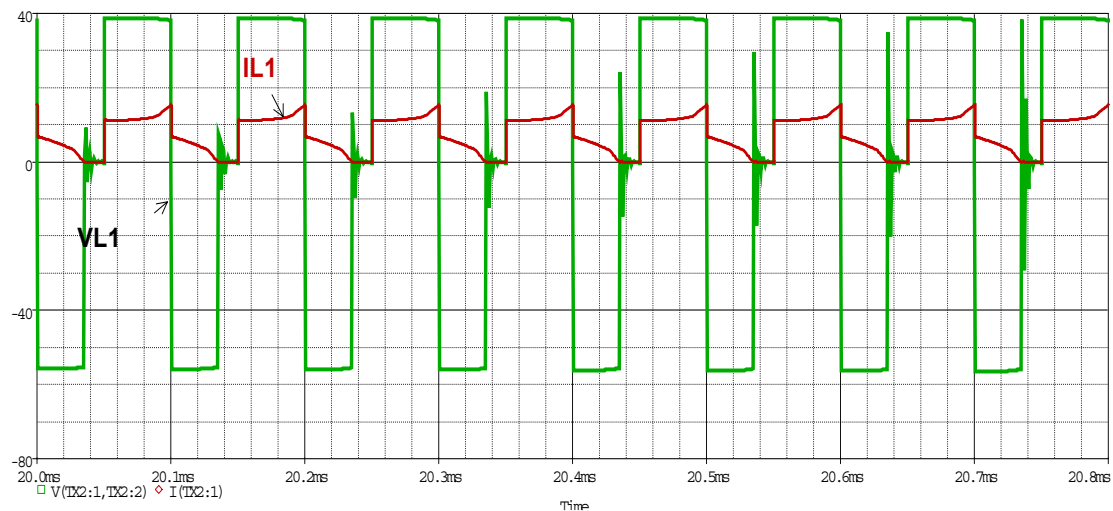


Figure 16. Voltage and current across L_1 .

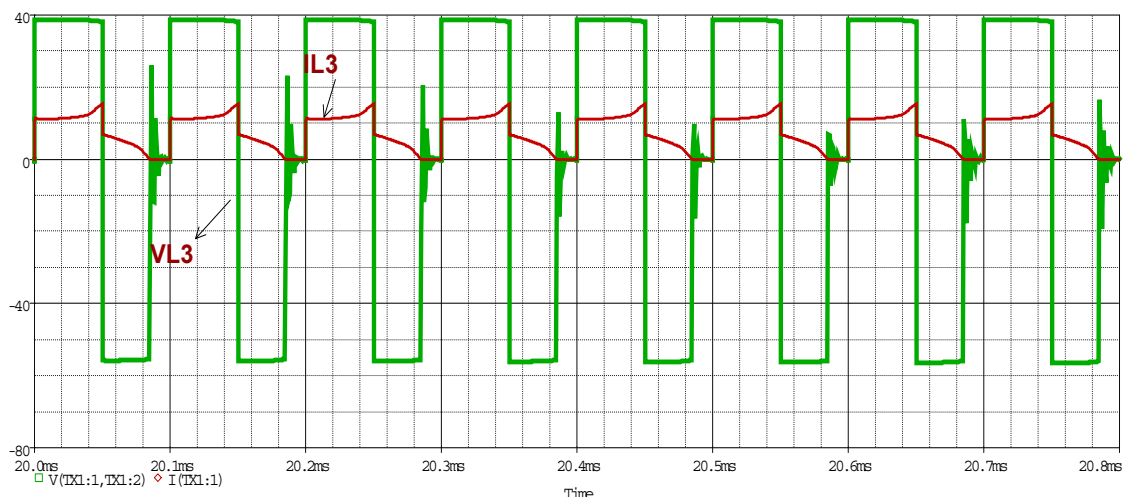


Figure 17. Voltage and current across L_3 .

For a 50% duty cycle, the control signals applied to the gate terminal will become complementary signals. Therefore, when the switch is closed, ideally zero volts will appear across its drain-to-source terminal. When the switch is open, the voltages at the battery terminals as well as the inductor voltages will appear across the switches. By increasing the duty cycle, high voltage peaks will appear across the switches because the inductor has to release its stored energy in a very limited amount of time. Figure 18 shows that the voltage across the switches is over 2-fold that of the battery input voltage. This is because the switch is turned on for a 50% duty cycle and the inductor cannot suddenly change directions and has to release the stored energy in less than half of the time period.

Figure 19 illustrates that the current is shared among the output diodes D_3 and D_6 . This current is fed into the load resistor in parallel with the filter capacitor. It is clear from the figure that both the output diodes are not conducting simultaneously. There is a very span of time where both the output diodes are in off-state therefore the load is being supplied by the output capacitor. The magnitude of the current through both the output diodes is the same, because the same valued components have been used for both phases. The current peaks through each diode are high. Therefore, they are filtered through the output capacitor. One of the main advantages of this circuit is that if any of the phase is

not conducting due to some failure, then power can be supplied to the load through the other phase without any interruption.

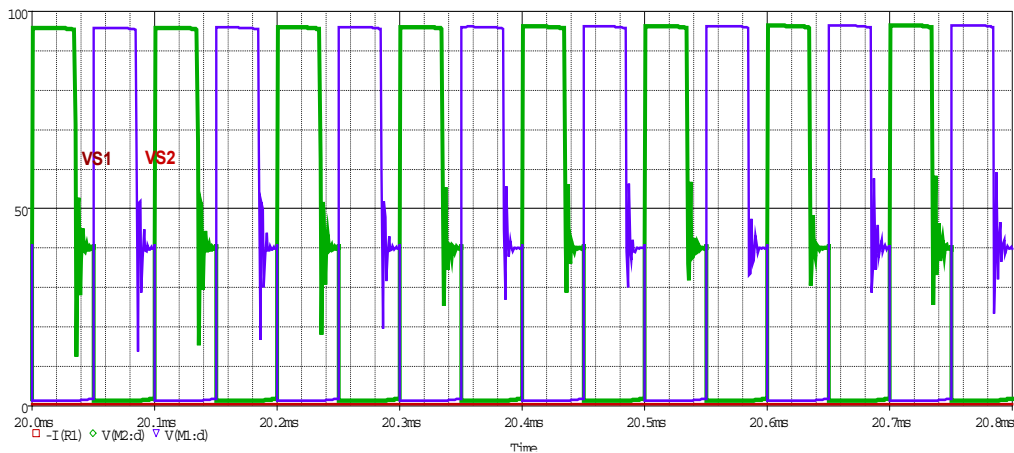


Figure 18. Voltage across switches (S_1 and S_2).

For 400 V of output voltage, a DC current of 0.71 flows through the load—the remaining current will charge the output capacitor C_6 . Figure 20 shows that the output current I_o is constant while the capacitor current flows in both the directions. The positive current shows that the capacitor C_5 is in the charging mode while the negative current illustrates that the current is supplied by the capacitor.

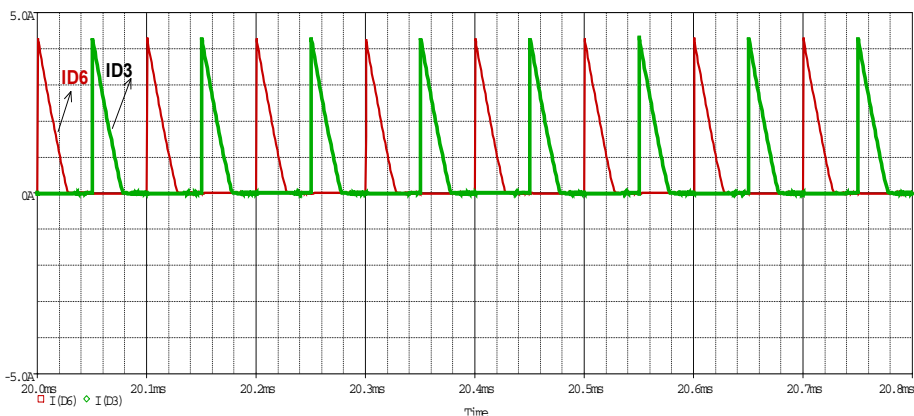


Figure 19. Current through D_3 and D_6 .

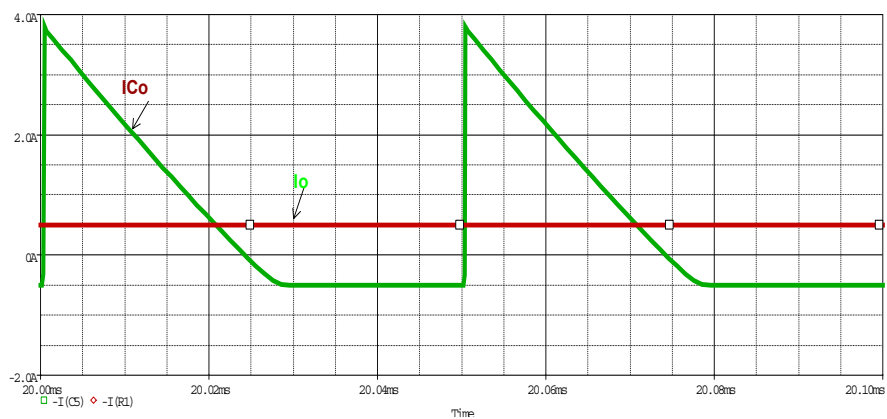


Figure 20. Waveforms for output capacitor current and output load current.

6.2. Buck Mode

In this mode of operation, the bus voltage of PV power systems, which is around 400 V, is required to be stepped down to store the energy in batteries. Therefore, to step down the voltage of the DC bus from 400 to 40 V it is mandatory to set the minimum duty cycle to 10%. Figure 21 illustrates the output voltage and output current of a bidirectional converter operated in the buck mode. The switch (S_3) used for the conversion of higher voltage to lower voltage must be rated for over 400 V because when the switch is in the non-conduction state, the high voltage link of the DC bus appears across it. Figure 22 shows the voltage across S_3 , in which 400 V are applied across the switch in the off state, while in the conduction state, it will act as a short circuit.

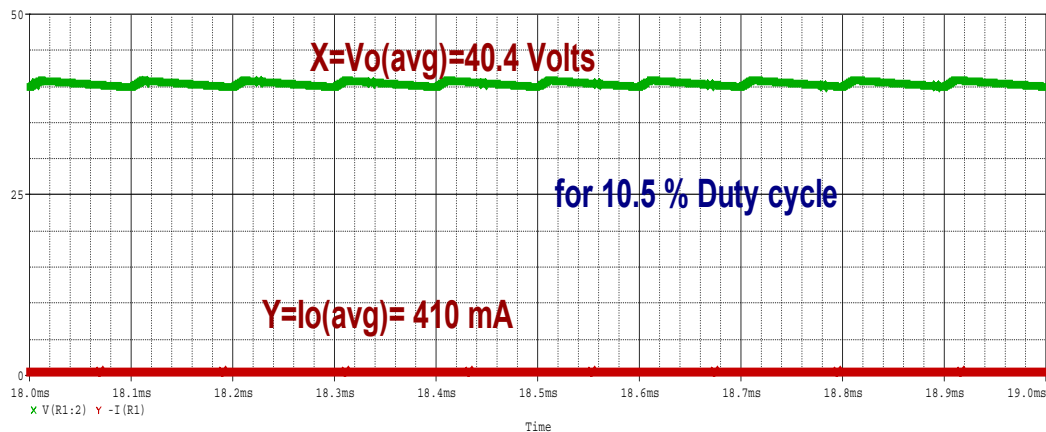


Figure 21. Voltage across battery and current through battery for a 10% duty cycle.

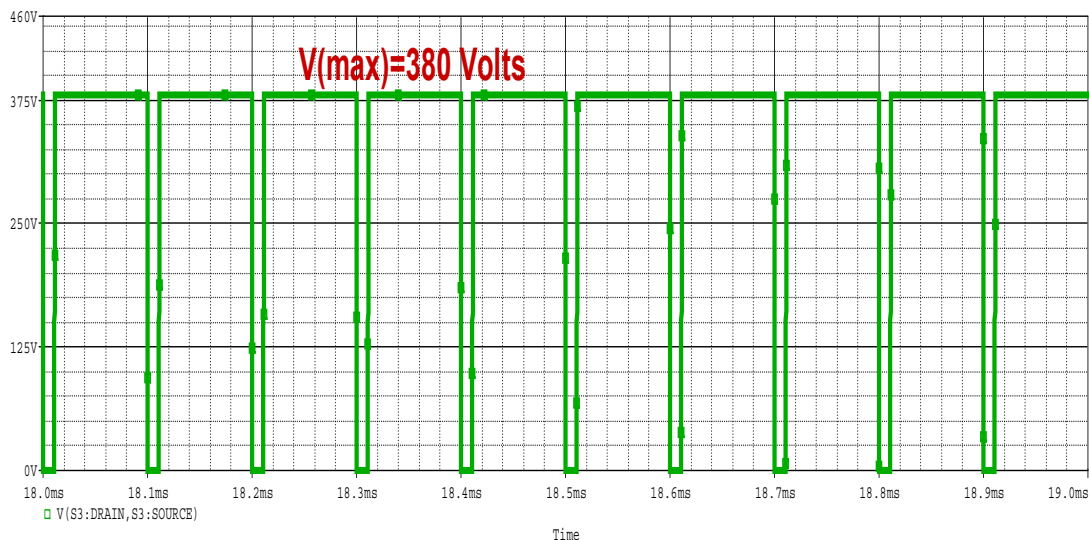


Figure 22. Voltage across S_3 .

6.3. Comparison with Conventional Converters

In previous section, the performance of the proposed converter was analyzed in detail. Here, we will compare our results with a conventional converter [28] and the results of a high-gain high-efficiency converter. In our proposed converter, the topology for the buck mode is similar to the conventional buck converter topology. Therefore, there is no need to compare the performance with any other converter. We will compare the results of the boost mode of operation in terms of voltage gain, magnitude of output voltage ripples, magnitude of output current ripples and the stress on power switches. A detail comparison with other converter topologies in terms of voltage gain,

Magnitude of output voltage/Current ripples and switching stress has been explained in Section 6.4.7 after the results of other converter topologies.

6.4. Results of [Novel High-Performance With High-Gain High-Efficiency DC–DC Converter and Conventional Boost Converter

The results in terms of Output current Ripples for Novel High Performance stand-alone Solar Pv system with high efficiency and high gain dc-dc converter [7] and conventional Boost converter [28] has been depicted in Figures 23 and 24 respectively.

6.4.1. Output Current Ripples of Novel High-Performance With High-Gain High-Efficiency DC–DC Converter and conventional Boost Converter

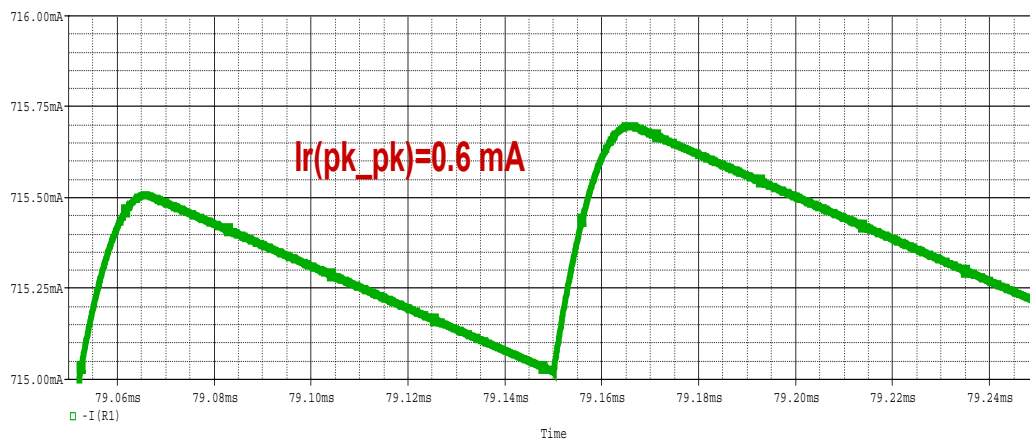


Figure 23. Magnitude of output current ripples for converter [7].

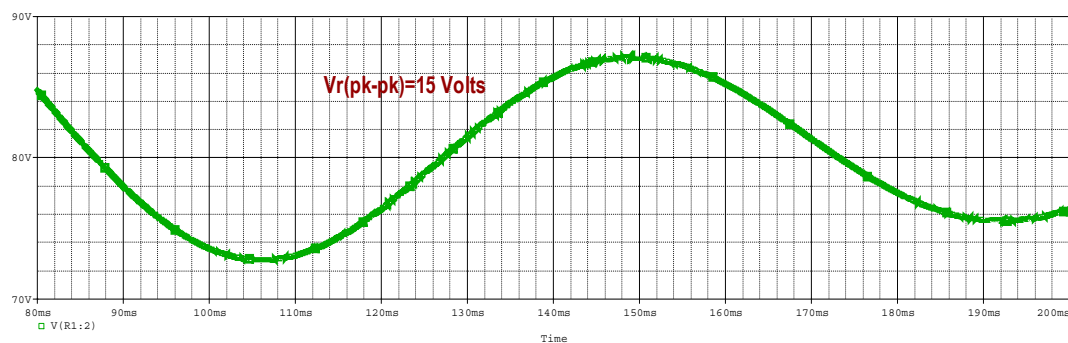


Figure 24. Magnitude of output current ripples for conventional boost converter [28].

6.4.2. Output Voltage Ripples of Novel High-Performance With High-Gain High-Efficiency DC–DC Converter and conventional Boost Converter

The results in terms of Output voltage Ripples for Novel High Performance stand-alone Solar Pv system with high efficiency and high gain dc-dc converter [7] and conventional Boost converter [28] has been depicted in Figures 25 and 26 respectively.



Figure 25. Magnitude of output voltage ripples for [7].

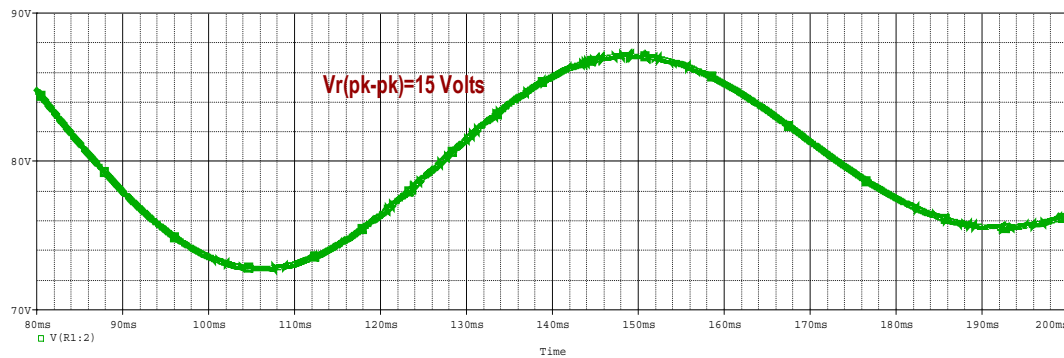


Figure 26. Magnitude of output voltage ripples for conventional boost converter [28].

6.4.3. Switching Stress of Novel High-Performance With High-Gain High-Efficiency DC–DC Converter and conventional Boost Converter

In order to determine switching stress of Novel High Performance stand-alone Solar Pv system with high efficiency and high gain dc-dc converter [7] and conventional Boost converter [28] voltage across and current through switches can be shown in the given figures below where Figure 27 shows current through switch ‘S’ of [7] while Figure 28 depicts Voltage across switch ‘S’ and Current through Switch ‘S’. Voltage across switch ‘S’ of [28] is depicted in Figure 29.

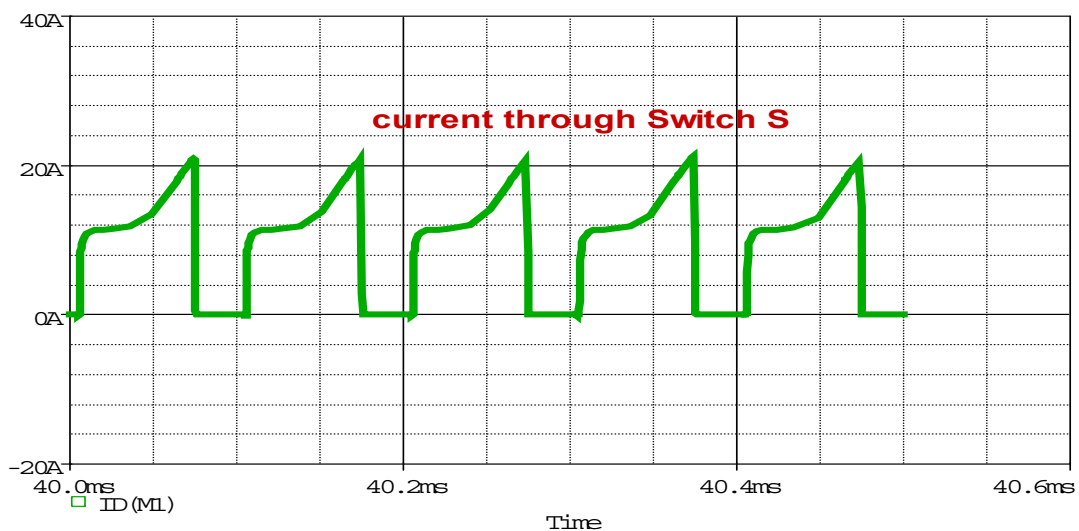


Figure 27. Current through switch “s” of the high-gain boost converter [7].

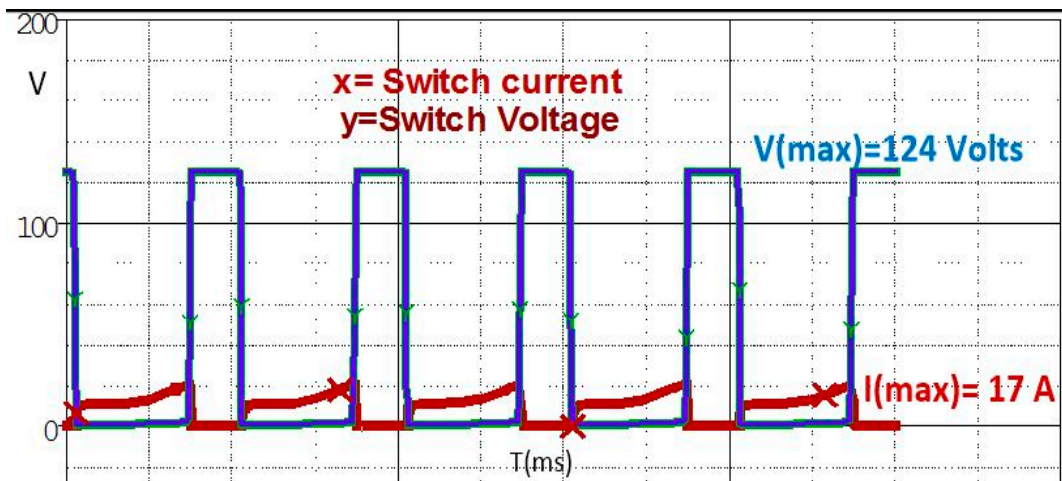


Figure 28. Voltage and current of switch “s” of the high-gain boost converter [7].

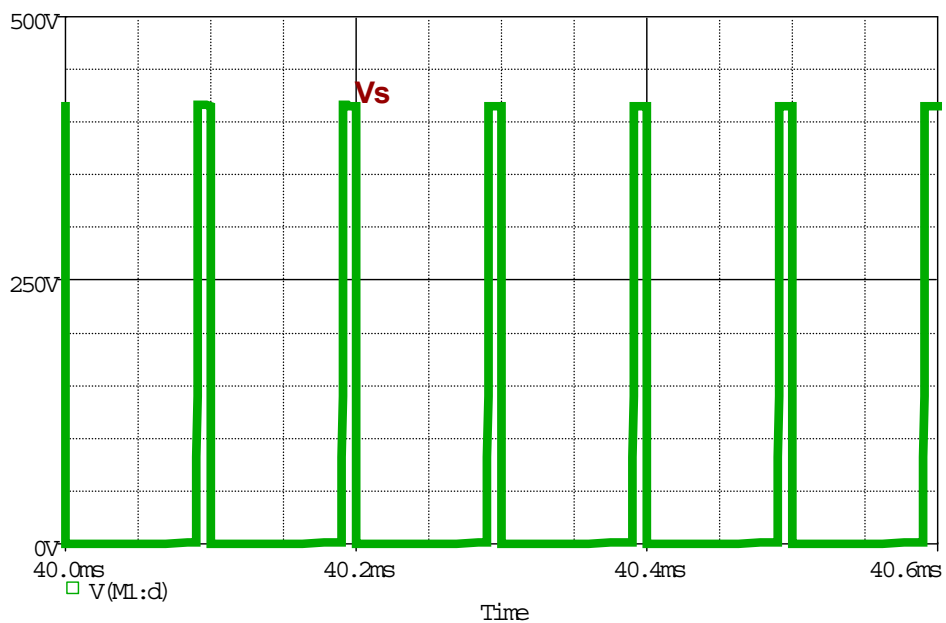


Figure 29. Voltage across switch “s” of the conventional boost converter [28].

6.4.4. Output Voltage of [Bidirectional Cûk Converter] for a 50% Duty Cycle

In order to compare the performance of Proposed Converter topology in terms of its Voltage gain with more topologies the output of famous bidirectional dc-dc converter topology (Cûk Converter) [28] has been depicted in Figure 30 for the same duty of 50 %, while the Input is constant for all topologies.

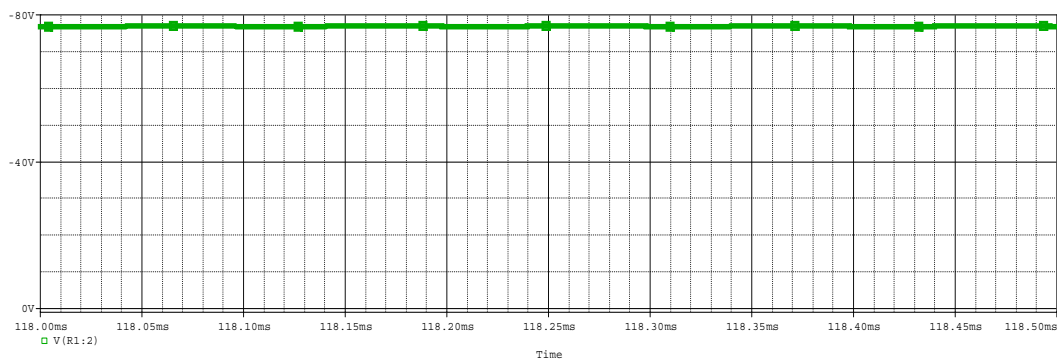


Figure 30. Output voltage of the bidirectional CUK converter [33].

6.4.5. Output Voltage and Current Ripples of Bidirectional Cûk Converter

The output voltage and current ripples for Bidirectional Cûk Converter [33] can be shown in Figures 31 and 32 respectively for the sake of comparison with the proposed converter topology.

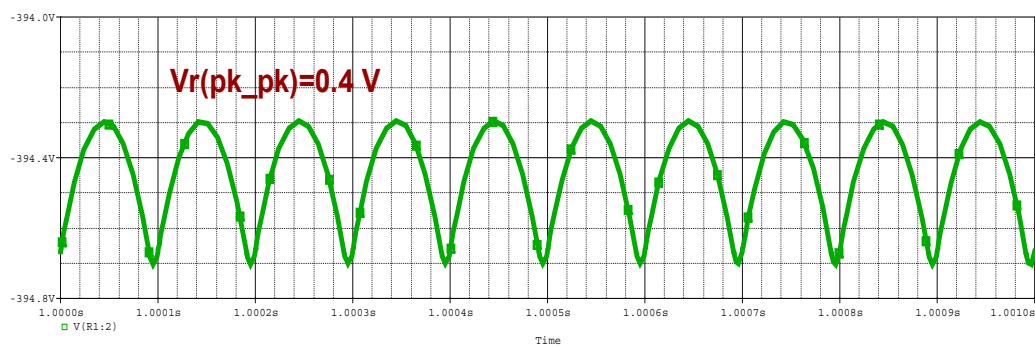


Figure 31. Output voltage ripples of the bidirectional Cûk converter [33].

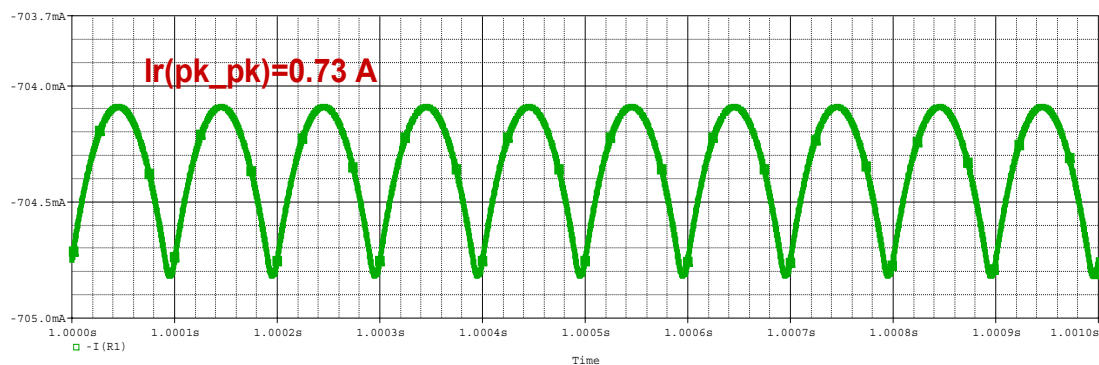


Figure 32. Output current ripples of the bidirectional Cûk converter [33].

6.4.6. Voltage and Current across Switch of Bidirectional Cûk Converter

For the comparison of switching stress of bidirectional Cûk Converter [33] with the proposed converter, Voltage across Switch 'S' and Current Through switch 'S' of [33] have been depicted in Figures 33 and 34.

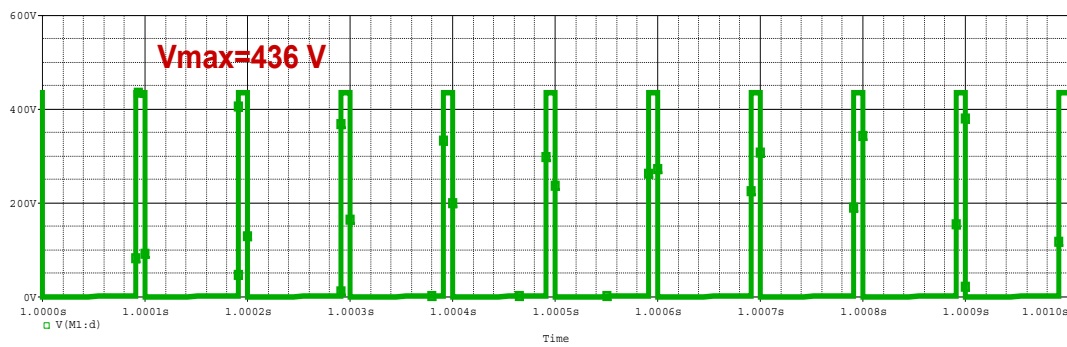


Figure 33. Voltage across switch “s” of the bidirectional CUK converter for a 400-V output [33].

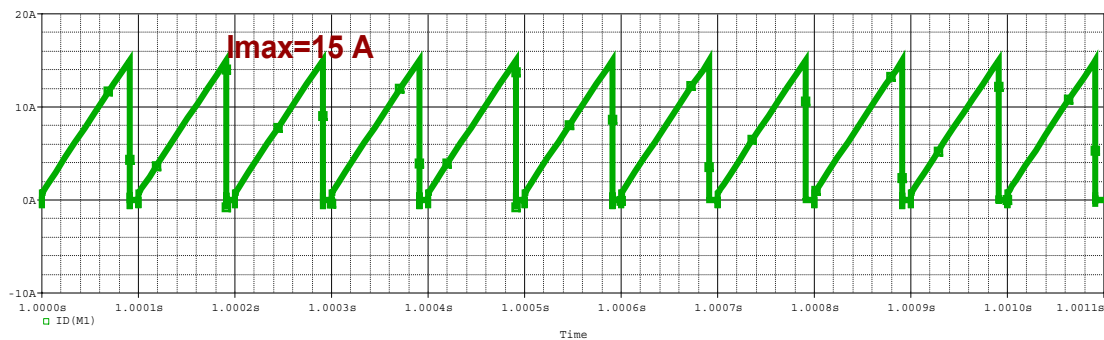


Figure 34. Current through switch “s” of the bidirectional CUK converter for a 400-V output [33].

6.4.7. Comparison with Other Converter Topologies

Voltage Gain Comparison

Figure 35 shows the voltage gain comparison of Proposed Converter topology with other converter topologies in the form of bar chart.

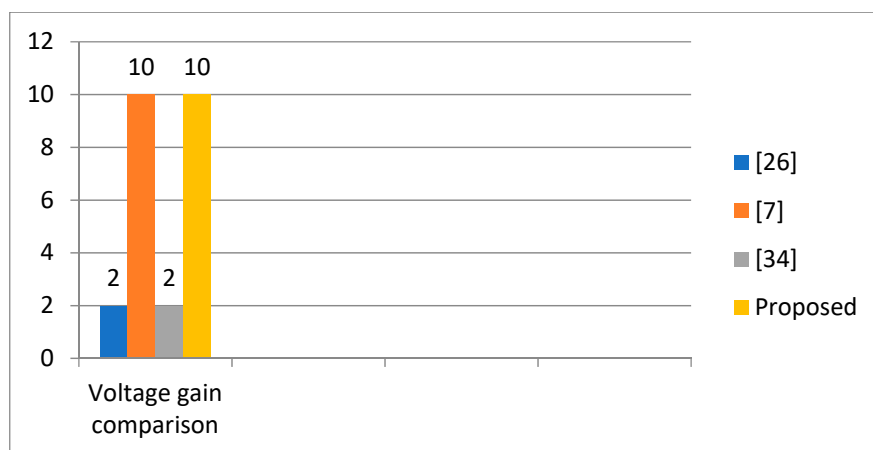


Figure 35. Voltage gain comparison.

Output Voltage (Ripples magnitude) Comparison.

Figure 36 shows the comparison chart of magnitude of ripple contents in output voltage of Proposed Converter topology with other converter topologies.

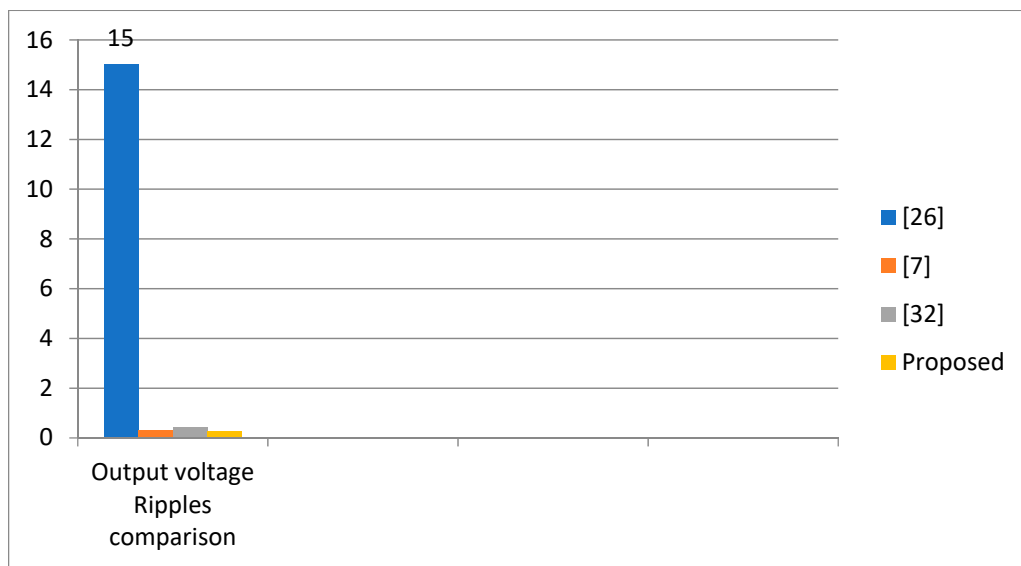


Figure 36. Voltage ripples magnitude comparison.

Output Current (Ripples magnitude) Comparison.

Figure 37 shows the comparison chart of magnitude of ripple contents in output current of Proposed Converter topology with other converter topologies.

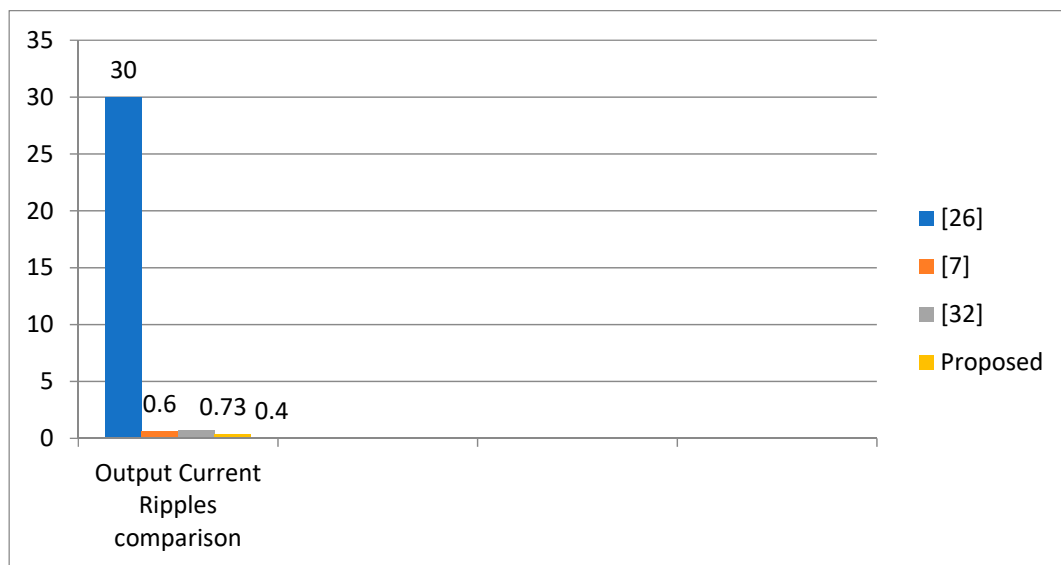


Figure 37. Current ripples magnitude comparison.

Switching Stress Comparison.

Figure 38 shows the comparison chart of switching stress of Proposed Converter topology with other converter topologies.

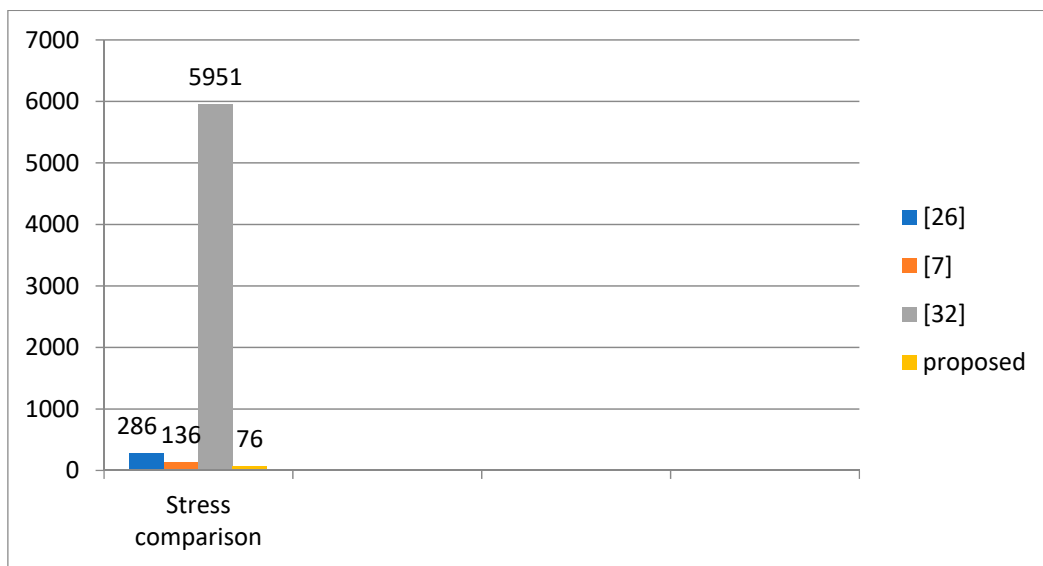


Figure 38. Switching stress comparison.

6.4.8. Load Regulation

Mathematically, load regulation can be given as

$$Load\ Regulation = \left| \frac{V_{NL} - V_{FL}}{V_{FL}} \right| \times 100\% \tag{26}$$

where

V_{NL} = the no-load output voltage

V_{FL} = the full-load output voltage

The no-load and full load output voltages are shown in Figures 39 and 40, respectively, and are measured as 401 and 387 V. Therefore, the % load regulation of the system is found to be

$$Load\ Regulation = 3.6\%$$

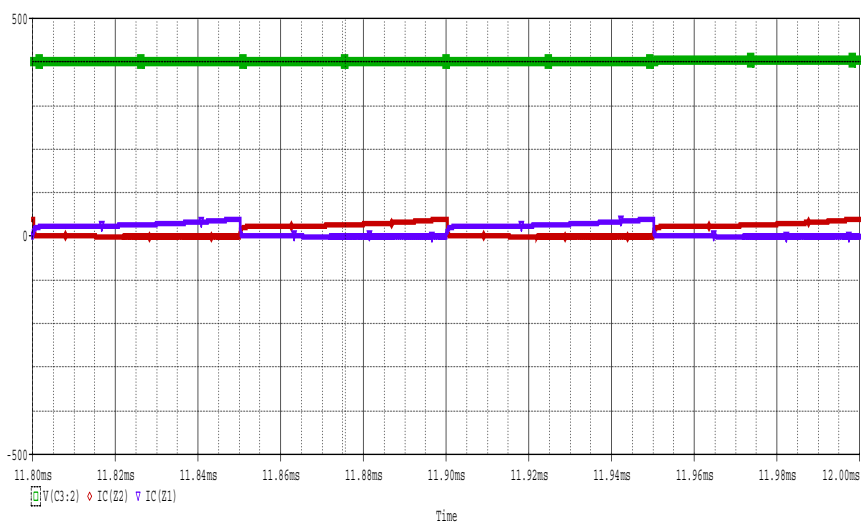


Figure 39. No-load output voltage.

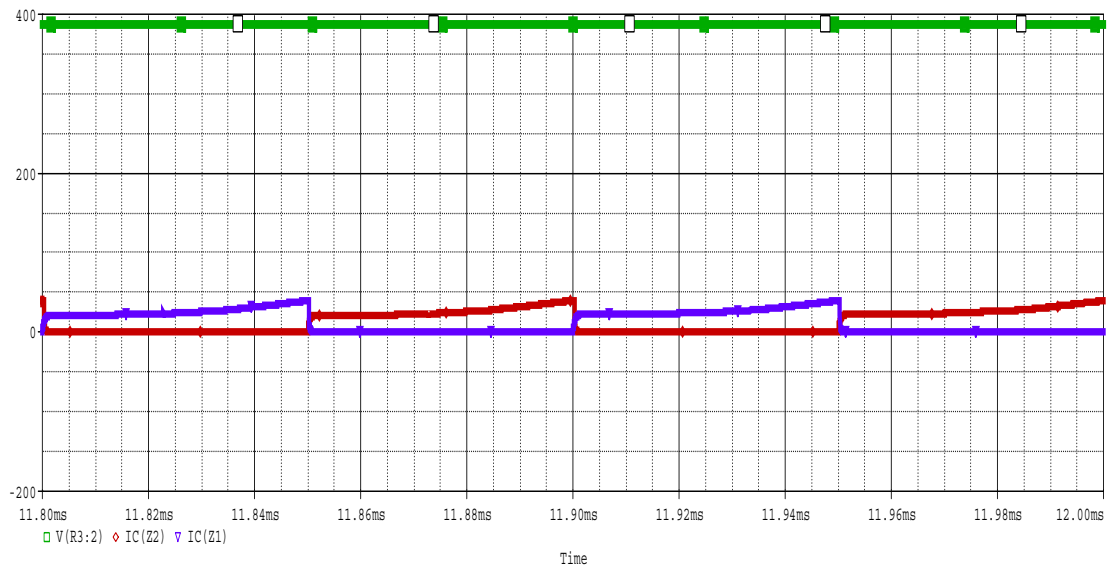


Figure 40. Full-load output voltage.

6.4.9. Transient Analysis

The proposed converter topology exhibits a good transient performance for various load conditions and it reaches the steady state condition in nanoseconds.

For a 1-KΩ Load

When a load of 1 KΩ is suddenly included in its output, the proposed converter topology will take 702 nanoseconds to bring itself into the steady state condition as depicted in Figure 41.

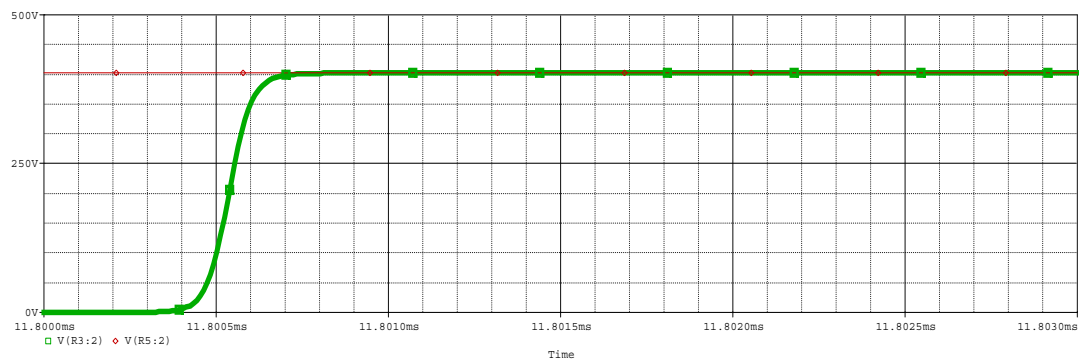


Figure 41. Transient performance for a 1-KΩ load.

For a 100-Ω Load

When a load of 100 Ω is suddenly included in its output, the proposed converter topology will take 732 nanoseconds to bring itself into the steady state condition as depicted in Figure 42.

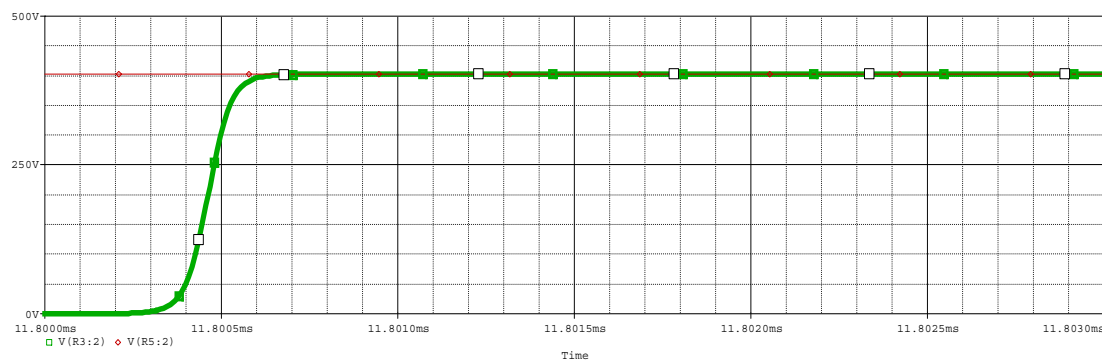


Figure 42. Transient performance for a 100- Ω load.

7. Conclusions

In this research, the main objectives were to explore and propose a novel topology for a bidirectional DC–DC converter with the features of high voltage gain when operated in the boost mode, without exposing the semiconductor switches to extreme duty cycles, low magnitude output voltage ripples, low stress on the semiconductor switches and increased the power density. With the above objectives in mind, the authors reviewed the available literature of isolated and non-isolated DC–DC converters and concluded that non-isolated DC–DC converters are more appropriate for the application of renewable energy sources and explicitly for stand-alone PV power systems. After reviewing the literature incorporating previous converter designs, a novel interleaved DC–DC converter has been proposed and, by selecting the optimum valued components, the design has been verified in ORCAD/PSPICE. The authors have achieved their main objectives in which a high voltage gain has been obtained for a duty cycle of 50% or less by changing the turn ration of coupled inductor. The magnitude of current and voltage ripples has been measured and compared with traditional converters and our proposed converter offers a low magnitude of ripples as compared to the present converters. Finally, a reduction in stress on the power switches has been achieved in this research, which is significant to increasing its efficiency.

Author Contributions: All authors contributed to the paper. A.H.: Conceptualization, Software, Writing; R.A.: Data curation, Validation, Funding acquisition; B.A.: Software, Methodology, Data curation; S.E.A.: Writing, validation, Investigation, Formal analysis; S.I.: Conceptualization, Review and editing.

Funding: No funding is available for any of the authors.

Conflicts of Interest: The authors have no conflict of interest to declare.

References

1. Renewable Energy and Other Alternative Energy Sources. In *Handbook Alternative Energy*; Chapter 12; ABC-CLIO: Santa Barbara, CA, USA, 2008; pp. 149–157.
2. Anderson, D. *Clean Electricity from Photovoltaics*; Archer, M.D., Hill, R.D., Eds.; London Imperial College Press: London, UK, 2001.
3. Markvart, T. *Solar Electricity*; Willey: New York, NY, USA, 2000.
4. Zhu, M. Simulation of PV array Characteristics and fabrications of microcontroller based MPPT J. In Proceedings of the 2012 International Conference on Electrical and Computer Engineering, Chengdu, China, 16–28 December 2010.
5. Zhao, Q.; Lee, F.C. High-efficiency, high step-up dc-dc converters. *IEEE Trans. Power Electron.* **2003**, *18*, 65–73. [[CrossRef](#)]
6. Lee, W.; Han, B.; Cha, H. Battery ripple current reduction in a three-phase interleaved dc-dc converter for 5 kW battery charger. In Proceedings of the 2011 IEEE Energy Conversion Congress and Exposition (ECCE), Phoenix, AZ, USA, 17–22 September 2011; pp. 3535–3540.
7. Moumita, D. Novel High-Performance Stand-Alone Solar PV System with High-Gain High-Efficiency DC–DC Converter Power Stages. *IEEE Trans. Ind. Appl.* **2015**, *51*, 4718–4728.

8. Li, W.; Lv, X.; Deng, Y.; Liu, J.; He, X. A Review of Non-Isolated High Step-Up DC/DC Converters in Renewable Energy Applications. In Proceedings of the 2009 Twenty-Fourth Annual IEEE Applied Power Electronics Conference and Exposition, Washington, DC, USA, 15–19 February 2009.
9. Kim, I.-D.; Paeng, S.-H.; Ahn, J.-W.; Nho, E.-C.; Ko, J.-S. New bidirectional ZVS PWM Sepic/Zeta dc-dc converter. In Proceedings of the IEEE ISIE, Vigo, Spain, 4–7 June 2007; Volume 56, pp. 555–560.
10. Jose, P.; Mohan, N. A novel bidirectional dc-dc converter with ZVS and interleaving for dual voltage systems in automobiles. In Proceedings of the IEEE IAS, Pittsburg, PA, USA, 13–18 October 2002; Volume 2, pp. 1311–1314.
11. Chen, G.; Xu, D.; Lee, Y.-S. A novel fully zero-voltage-switching phase-shift bidirectional dc-dc converter. In Proceedings of the IEEE APEC, Anaheim, CA, USA, 4–8 March 2001; Volume 2, pp. 974–979.
12. Caricchi, F.; Crescimbin, F.; Noia, G.; Pirolo, D. Experimental study of a bidirectional dc-dc converter for the dc link voltage control and the regenerative braking in PM motor drives devoted to electrical vehicles. In Proceedings of the IEEE APEC, Orlando, FL, USA, 13–17 February 1994; pp. 381–386.
13. Zhang, J.; Lai, J.-S.; Kim, R.-Y.; Yu, W. High-power density design of a soft switching high-power bidirectional dc-dc converter. *IEEE Trans. Power Electron.* **2007**, *22*, 1145–1153. [[CrossRef](#)]
14. Urciuoli, D.P.; Tipton, C.W. Development of a 90 kW bi-directional dc-dc converter for power dense applications. In Proceedings of the IEEE APEC, Dallas, TX, USA, 19–23 March 2006; pp. 1375–1378.
15. Tseng, K.C.; Liang, T.J. Novel high-efficiency step-up converter. *IEE-Elect. Power Appl.* **2004**, *151*, 182–190. [[CrossRef](#)]
16. Zhao, Q.; Tao, F.; Lee, F.C. A front-end DC/DC converter for network server applications. In Proceedings of the IEEE PESC'01, Vancouver, BC, Canada, 17–21 June 2001; pp. 1535–1539.
17. Zhao, Q.; Lee, F.C. High performance coupled-inductor DC-DC converters. In Proceedings of the IEEE APEC'03, Miami Beach, FL, USA, 9–13 February 2003; pp. 109–113.
18. Gules, R.; Pfitscher, L.L.; Franco, L.C. An interleaved boost DC-DC converter with large conversion ratio. In Proceedings of the IEEE ISIE'03, Rio de Janeiro, Brazil, 9–11 June 2003; pp. 411–416.
19. Franco, L.; Gules, C.R.; Pfitscher, L.L. A new high static gain nonisolated DC-DC converter. In Proceedings of the IEEE PESC'03, Acapulco, Mexico, 15–19 June 2003; pp. 1367–1372.
20. Li, W.; He, X. ZVT Interleaved Boost Converters for High-Efficiency, High-Step-Up DC/DC Conversion. *IET-Elect. Power Appl.* **2007**, *1*, 284–290. [[CrossRef](#)]
21. Li, W.; He, X. An Interleaved Winding-Coupled Boost Converter with Passive Lossless Clamp Circuits. *IEEE Trans. Power Electron.* **2007**, *22*, 1499–1507. [[CrossRef](#)]
22. Li, W.; He, X. A Family of Interleaved DC/DC Converters Deduced from a Basic Cell with Winding-Cross-Coupled Inductors (WCCIs) for High Step-Up or Step-Down Conversions. *IEEE Trans. Power Electron.* **2008**, *22*, 1499–1507. [[CrossRef](#)]
23. Lee, Y.S.; Chiu, Y.Y. Zero-current-switching switched capacitor bidirectional DC-DC converter. *IEE Proc. Electr. Power Appl.* **2005**, *152*, 1525–1530. [[CrossRef](#)]
24. Pham, C.; Kerekes, T.; Teodorescu, R. High efficient bidirectional battery converter for residential PV systems. In Proceedings of the 2012 3rd IEEE International Symposium on Power Electronics for Distributed Generation Systems (PEDG), Aalborg, Denmark, 25–28 June 2012; pp. 890–894.
25. Guo, X.; Wen, X.H.; Qiao, E. A DSP Based Controller for High Power Dual-Phase DC-DC Converters. In Proceedings of the CES/IEEE 5th International Power Electronics and Motion Control Conference (IPEMC 2006), Shanghai, China, 14–16 August 2006; Volume 1, pp. 1–5.
26. Elankurisil, S.A.; Dash, S.S. Comparison of isolated and nonisolated bi-directional dc-dc converters. *J. Eng.* **2011**, *21*, 2341–2347.
27. Dragičević, T.; Lu, X.; Vasquez, J.C.; Guerrero, J.M. DC microgrids+Part I: A review of control strategies and stabilization techniques. *IEEE Trans. Power Electron.* **2016**, *1*, 4876–4891.
28. Prabhala, V.A.K.; Fajri, P.; Gouribhatla, V.S.P.; Baddipadiga, B.P.; Ferdowsi, M. A DC-DC converter with high voltage gain and two input Boost stages. *IEEE Trans. Power Electron.* **2016**, *31*, 4206–4215. [[CrossRef](#)]
29. Ghosh, A.; Banerjee, S. Study of complex dynamics of DC-DC buck converter. *Int. J. Power Electron.* **2017**, *8*, 323–348. [[CrossRef](#)]
30. Nasir, M.; Khan, H.A.; Hussain, A.; Mateen, L.; Zaffar, N.A. Solar PV-Based Scalable DC Microgrid for Rural Electrification in Developing Regions. *IEEE Trans. Sustain. Energy* **2018**, *9*, 390–399. [[CrossRef](#)]

31. Lakshmi, M.; Hemamalini, S. Nonisolated High Gain DC-DC Converter for DC Microgrids. *IEEE Trans. Ind. Electron.* **2018**, *65*, 1205–1212. [[CrossRef](#)]
32. Chung, H.Y.; Poon, F.N.K.; Liu, C.P.; Pong, M.H. Analysis of buck-boost converter inductor loss using asimpleonline B-H curve tracer. In Proceedings of the 15th Annual IEEE Applied Power Electronics Conference and Exposition (APEC 2000), New Orleans, LA, USA, 6–10 February 2000; Volume 2, pp. 640–646.
33. Mallikarjuna Reddy, B.; Samue, P. A Comparative Analysis of Non-Isolated Bi-directional DC-DC Converters. In Proceedings of the IEEE International Conference on Power Electronics, Intelligent Control and Energy Systems (ICPEICES-2016), Delhi, India, 4–6 July 2016.



© 2019 by the authors. Licensee MDPI, Basel, Switzerland. This article is an open access article distributed under the terms and conditions of the Creative Commons Attribution (CC BY) license (<http://creativecommons.org/licenses/by/4.0/>).